Article

Optimal Inverter Control Strategies for a PV Power Generation with Battery Storage System in Microgrid

Md Jahidur Rahman [1,*] , Tahar Tafticht [1], Mamadou Lamine Doumbia [2] and Iqbal Messaïf [3]

1   Department of Engineering, Université du Québec en Abitibi-Témiscamingue, Rouyn-Noranda, QC J9X 5E4, Canada; tahar.tafticht@uqat.ca
2   Department of Electrical and Computer Engineering, Université du Québec à Trois-Rivières, Trois-Rivières, QC G8Z 4M3, Canada; mamadou.doumbia@uqtr.ca
3   Department of Electrical Engineering, Université des Sciences et de la Technologie Houari Boumediene, Alger 16111, Algeria; imessaif@usthb.dz
*   Correspondence: mdjahidur.rahman@uqat.ca

Abstract: Power generation from Renewable Energy Sources (RESs) is unpredictable due to climate or weather changes. Therefore, more control strategies are required to maintain the proper power supply in the entire microgrid. This paper presents a simulation scheme utilizing a solar system instanced by Photovoltaic (PV) panels coupled to the grid, loads, and an energy storage device. At first, modeling the PV panels cell and their operation were analyzed. The synthesis of the adaptive notch filter was designed to compensate for the input currents. The power converter's/inverter's efficiency and control facility allowed us to link the energy storage system with an electrical grid. Several simulations were accomplished consistently with nonlinear control techniques for the simple inverter, multi-variable filter, notch filter, and without a filter. Finally, the performances of the nonlinear controller with various filters were carried out to regulate the DC bus of the proposed grid. The advantage of these controllers is compensating the reactive power and harmonic currents to obtain a disturbance-free power network. The overall installations and simulations were established using the Matlab/Simulink software.

Keywords: photovoltaic energy; storage system; nonlinear control; power converter/inverter; harmonic currents; reactive power

1. Introduction

The current structure of electrical grids is a centralized architecture wherein energy production is concentrated at specific points and then distributed to consumers [1–3]. During the last three decades, renewable energies have increased on the surface of our planet. This trend has gradually accelerated, particularly following the signing of the Kyoto Protocol, which requires many countries to limit their gas emission. Indeed, solar energy production in the world has increased 20-fold in ten years [4]. Efforts are underway to improve the competitiveness of solar panels in terms of performance and cost. The materials used in the manufacture are evolving, with the panels possessing a more critical yield. The main disadvantage of solar energy is that it varies irremediably according to weather conditions [5]. For example, the power provided by the PV panels is noticeably reduced in winter, night, or rainy weather. However, the development of photovoltaic systems has highlighted several factors directly affecting the performance of this technology. Studies have made it possible to emphasize the influence of partial shading and the impact of the increase in temperature on the efficiency of photovoltaic solar systems [6].

Many researchers have proposed technical solutions to reduce or eliminate these phenomena. The ultimate goal is to make the photovoltaic panels work at their maximum power points under any environmental conditions [7]. The partial shading on solar panels is usually caused by obstacles close to photovoltaic installations, such as trees, tall chimneys,

walls, etc. Most of these obstacles are permanent, predictable, and detected at certain times of the year due to the sun's path [8,9]. We also notice short-lived and unpredictable partial shading due to passing clouds, bird droppings, snow, dust, etc.

When the solar radiation is constant, the photovoltaic cell is likened to a diode that operates in direct bias. Since it's connected in series, the cells are required to drain the current. However, they cannot do so because some PV cells receive partial shading. Once partial shading occurs, the short circuit current of the shaded cells drops dramatically, which leads shaded cells to operate in reverse bias [3]. In the reverse bias region, the PV solar cell will dissipate power in the form of heat that creates a hot spot and can damage the shaded PV solar cells [9]. Advanced MPPT methods have been developed to detect the global maximum point when partial shading occurs with high accuracy and acceptable speed. Speed and accuracy are essential parameters when choosing the MPPT techniques [3]. These methods can be listed in three categories: linear search methods, artificial intelligence methods, and the metaheuristic approach [10]. The combination of the two steps generally develops linear search methods. The first step allows a sweep to find the region that contains the global maximum point. The second step uses one of the conventional MPPT techniques to find the location of the maximum power point with high accuracy.

The experimental results show that technology is more effective, particularly when weather conditions change suddenly. The disadvantage of this technology is that it does not guarantee rapid convergence during permanent partial shading. We can also mention the Global Maximum Power Point Tracking (GMPPT) algorithm. The advantage of this technique is that it can be applied in photovoltaic systems whose electrical characteristics are unknown. According to [11], this technique is better suited to building-integrated photovoltaic systems with inverters mostly mounted in strings. Artificial intelligence methods such as artificial neural networks and fuzzy logic controllers are also used. The technique using artificial neural networks can effectively track the global maximum point under any sunlight condition. Its advantage is that depending on the weather conditions, it can use some or all of its input parameters. The disadvantage of this technique is that it is not accurate under all partial shade conditions without periodic adjustment [3]. The fuzzy logic controller method allows fast and precise convergence even when the sunshine varies suddenly. The advantage of the method is that it does not require mathematical modeling of the system.

However, according to [12], the table of logic rules described in [13] largely depends on the designer's experience and prior knowledge of how the photovoltaic system works. The metaheuristic approach has the well-known Particle Swarm Optimization (PSO) technique. This technique finds a function's optimal value in a predefined search space. It is inspired by the social behavior of a large group of birds and a fish gathering [11,12]. The PSO is estimated to be relatively fast and accurate, with an error of 4% from experimental results. An improved version of this method, called Adaptive Perceptive PSO, has been proposed, providing more accurate results (3% error).

The other exciting technique is the Fibonacci Search method. It uses the sequence of Fibonacci numbers to track the global maximum point under uniform and non-uniform insulation conditions. Its tracking rate is acceptable according to the experimental results, but it sometimes fails when we have a power-voltage characteristic curve $P_{pv} = f(V_{pv})$ with multiple peaks. On the other hand, its slowness constitutes a limit for its implementation. We can also quote that the Modified Firefly Algorithm [13] can significantly reduce the global maximum tracking time even though its efficiency is slightly lower than that of the Firefly Algorithm. Many other techniques have recently been listed in the literature. In [14], the following methods are mentioned: Evolutionary algorithm, Genetic Algorithm, and Differential Evolution. There are also other lesser-known techniques for reconfiguring photovoltaic panels that allow maximum power to be achieved. However, these techniques require the installation of sensors, switches, and complex control algorithms to dynamically reconfigure the photovoltaic field [15] during partial shading conditions.

These reconfigurations can be partial or complete. The Partial reconfiguration foresees part of the photovoltaic cells of the solar field being fixed, and the other part can be reconfigured. The entire reconfiguration predicts that all the photovoltaic cells of the solar area are reconfigurable. Research has already been carried out in the past and proposed partial or complete reconfiguration algorithms. We can name the unbalance topology of photovoltaic cells [16], the model using mathematical formulas [17], and the dynamic programming algorithm [18]. However, all these methods use switches, which generate power losses. The algorithm for determining optimal connections [19], a new approach, uses busbars to change the positions of the photovoltaic cells between them. This has the advantage of minimizing power losses for switches. Other more recently developed techniques, such as the Futoshiki configuration, are based on the logic of puzzles. In this approach, the physical location of the photovoltaic modules changes, but the electrical connections of the modules are unchanged. The study results show that the Futoshiki technique generates greater power for all shading conditions than the total-cross-tied configuration [20,21]. The disadvantage of the method is that it cannot extract the maximum power from the photovoltaic system. It will be necessary to develop an algorithm that allows this technique to optimize the pursuit of the global maximum point [14].

Control strategies of an inverter are also developed to minimize the harmful effects of partial shading, especially in high-power photovoltaic systems. The control strategy named Mitigation Control Against Partial Shading Effects (MICAPAS) allows isolated photovoltaic power plants to regulate the frequency of partial shading without resorting to energy storage. However, according to [22], this strategy is only effective for huge photovoltaic power plants. We have noted in the literature that a more practical version of the sub-Module Integrated Converters (MICs) control strategy has been implemented. It also makes it possible to minimize power losses due to partial shading and mismatch between solar panels [23]. Sliding mode control is also a widely used strategy. Its principle consists of bringing a system's state trajectory towards the sliding surface and making it commute around this one until the point of equilibrium. It has the advantage of being stable and easy to implement [24,25]. To improve the robustness of this technique, the Proportional-integral Control and the sliding mode control have been developed [26]. Sliding mode control is one of the nonlinear control techniques. Another nonlinear technique is drop control. Although it has limitations, it is one of the most widely used techniques to guarantee the reliability of the power network [27,28]. Thus variants of this control technique have been implemented to optimize it [29,30].

In PV power generation, the inverter systems introduce some energy losses during the conversion of DC power generated by the PV panels to AC power used in most electrical systems. These losses can reduce the overall efficiency of the system. Furthermore, the efficiency of inverters can vary depending on their design, size, and load conditions [31]. In some cases, PV systems are oversized by installing inverters with higher capacities than necessary to accommodate future expansions or increase system flexibility. However, oversizing the inverter without appropriate load management or battery storage can lead to inefficient utilization of generated power and may result in increased costs without proportional benefits [5,9,32]. The inverter-based PV systems rely on grid-connected operation to ensure stable voltage and frequency levels. However, sudden variations in PV power generation can introduce voltage and frequency fluctuations, and increase the Total Harmonic Distortion (THD) of the inverter which has a huge impact to maintain the stability of the local grid [33]. This issue becomes more pronounced when a significant number of PV systems are connected to the same grid. The grid codes and standards are in place to address these challenges, but they can impose additional requirements and costs on PV system installations [34]. Also, inverter-based PV systems with battery storage often rely on the grid as a backup source of power or to supply excess electricity during periods of high demand. If the grid experiences an outage, these systems may not be able to operate independently unless they incorporate additional equipment such as backup generators or specialized grid-forming inverters. Grid dependence can limit the system's resilience

and reliability, especially in areas with unreliable or weak grid infrastructure [32,35]. It's worth noting that these deficiencies mostly are in inverter-based PV power generation systems with battery storage and can vary depending on the specific components, system design, and grid conditions. Ongoing research and technological advancements continue to address these limitations and improve the performance and reliability of inverter-based PV systems.

Thus, this paper presents photovoltaic technology, extracting electrical energy using the boost converter to determine the MPPT. The power generated by the PV panel was connected to the grid with a battery storage system ensured by the DC/AC converter to maintain the unbalanced nonlinear load. This converter interfaced with the grid, which corrected the components and blocks the pollution of the grid through its control strategies. The simulation tests were carried out with a simple nonlinear controller and integrated into the multi-variable and notch filters. Finally, we simulated the inverter using a nonlinear controller without a filter and compared the results to determine the best controller that performs better. The main contributions of this paper are designing the control scheme for an inverter/rectifier to help the batteries store/supply a desired amount of energy at maximum speed; designing DC/AC converters to maintain the unbalanced nonlinear load of the PV-based battery storage system; modifying the adaptive notch filter to adequately compensate the input currents and perform an inverse transformation before injecting them at the output; and reducing the (THD) rate of the inverters to enhance the efficiency of the power grid.

The rest of the paper is organized as follows: Section 2 describes the modeling of a solar photovoltaic cell. Section 3 presents the photovoltaic system connected to the power grid. The simulation results and performance of the nonlinear controller with different types of filters are presented in Section 4. The comparison of nonlinear controllers with various filters is analyzed in Sections 5 and 6 concludes the paper.

2. Modeling of a Solar Photovoltaic Cell

A single photovoltaic cell cannot provide enough power to supply a load or the electrical grid. Therefore, it is necessary to combine these solar cells to generate more power. A series combination of the cell will increase the solar panel output voltage, while a parallel combination will increase the current supplied to the load. Here, N_P and N_S represent the number of cells in parallel and series. Now the expression of the current I_{PV} becomes [36]:

$$I_{pv} = N_P I_{SC} - \left(e^{\frac{I_{pv} R_S}{N_P V_T} + \frac{V_{pv}}{N_S V_T}} - 1 \right) I_0 - I_{pv} \frac{R_S}{R_p} - \frac{V_{pv}}{R_p} \tag{1}$$

where I_{pv} represents the current for a photovoltaic cell; I_{sc} represents the short-circuit current of a cell; I_0 represents the diode reverse bias current; V_{pv} represents the voltage for a photovoltaic cell; V_T represents the thermal voltage of a cell; N_P and N_S represent the number of cells in parallel and series; R_p represents the resistance losses by recombination of the carriers due to the structural defects of the material; R_s represents the resistance losses by joule effects in the semiconductor and the losses through the grids and the bad ohmic contacts of the cell. The amount of solar radiation affects the production of carrier charge in the PV module, subsequently affecting the generated current.

The following equation describes the current I_{pv} with the influence of the cell temperature:

$$I_{pv} = I_{sct} - \left(e^{\frac{\frac{I_{pv} R_S}{N_P} + \frac{V_{pv}}{N_S}}{V_T}} - 1 \right) I_{0s} N_p - I_{pv} \frac{R_S}{R_p} - \frac{V_{pv}}{R_p} \tag{2}$$

$$I_{os} = \left(\frac{T}{T_t} \right)^3 I_{or} - \left(e^{(\frac{1}{T_r} - \frac{1}{T}) \frac{q E_{G0}}{k \beta}} - 1 \right) \tag{3}$$

$$I_{sct} = \frac{G}{1000}[(T - 298.15)K_I + I_{sc}] \tag{4}$$

where T is the cell's operating temperature in Kelvin and T_r is the reference temperature (298.18 K); E_{G0} is the silicon's bandwidth (1.12 eV); β is the ideality factor (1740); I_{os} is the reverse saturation current of the cell; I_{or} is the saturation current of the cell; q is the charge of electrons.

The selection of solar cells significantly contributes to better efficiency in the overall power grid. Indeed, the temperature and the level of sunlight can affect the solar panel's performance. In order to distinguish the modified value of the current and the voltage of the solar panel due to a temperature change, the following characteristic curves $I_{pv} - V_{pv}$ and $P_{pv} - V_{pv}$ are plotted using Equations (2)–(4) and can also be written as follows:

$$P_{pv} = V_{pv}I_{pv} = V_{pv}\left(I_{sct} - \left(e^{\frac{\frac{I_{pv}R_S}{N_p} + \frac{V_{pv}}{N_S}}{V_T}} - 1\right)I_{0s}N_p - I_{pv}\frac{R_S}{R_p} - \frac{V_{pv}}{R_p}\right) \tag{5}$$

The following curves are obtained (with 15 photovoltaic modules in series and 50 in parallel). Figure 1 shows the I-V and P-V curves of PV modules with a temperature variation.
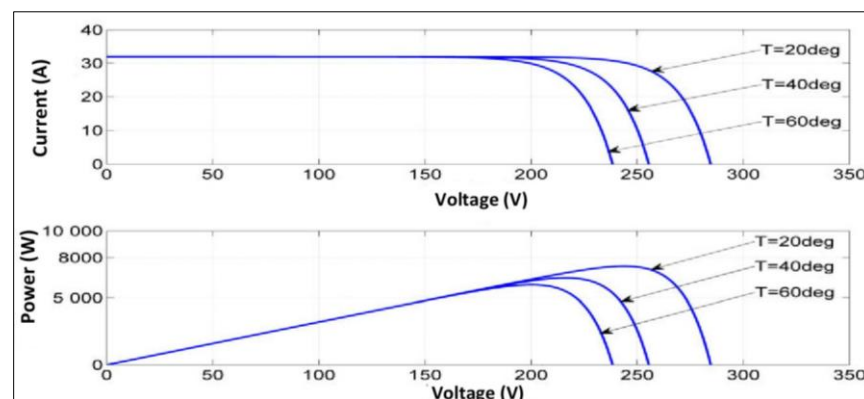
Figure 1. I-V and P-V curves of PV modules with temperature variation.

It is observed that the power produced by the panel decreases at high temperatures. The characteristics of the solar panel according to the radiation $G = 600$, 800, and 1000 W/m^2 are shown in Figure 2.
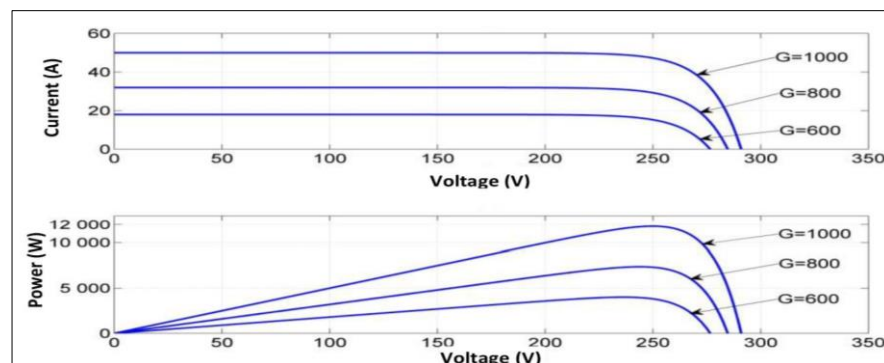

Figure 2. I-V and P-V curves of PV modules with the variation of sun radiation.

3. Photovoltaic System Connected to the Power Grid

The MPPT is a principle technique for tracking the maximum power point of a nonlinear power generator. This control technique forces the generator to work at its Maximum Power Point (MPP). Indeed, this operation makes it possible to obtain the best power effi-

ciency of the photovoltaic system. A photovoltaic generator has a nonlinear characteristic of $I = f(U)$. Consequently, the power supply will differ according to the load for the same lighting. Therefore, an MPPT controller makes it possible to control the static converter connecting to the load and the photovoltaic panel to supply the maximum power to the load permanently. There are different methods to get to this point. Generally, each of these methods has been made for a specific application. The accuracy and robustness of these controllers depend on some parameters (i.e., sampling rate, system voltage, temperature compensation, noise, and filtering). For our application, the Perturb and Observe (P&O) method is used to get MPPT from the PV panel. Here, the inverter is placed downstream from the boost converter and upstream from the grid. Its principal function is to deliver the alternating currents and voltages from a DC power source. Figure 3 shows the generic circuit diagram of a boost converter. This DC-DC converter, also called a parallel chopper, is a switching power supply that increases the initial DC voltage. Therefore it makes it possible to impose a current, which will be determined by the MPPT algorithm.
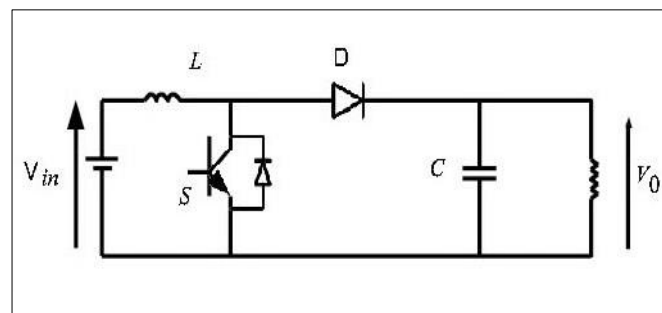
Figure 3. Generic circuit diagram of a boost converter.

For current regulations, we will use the dynamic current equation:

$$V_{in} - (1 - d)v_c = L\frac{dI_L}{dt} \tag{6}$$

We use a proportional-integral (PI) controller to regulate the current, the new input u (which represents the output of the regulator), and it is defined as follows:

$$u = L\frac{dI_L}{dt} \tag{7}$$

Using the Laplace transform, we obtain

$$u = S{\cdot}L{\cdot}I_L \tag{8}$$

Lets G is the open loop current transfer function defined as follows:

$$G = \frac{1}{SL} = \frac{I_L}{u} \tag{9}$$

The controller will generate the boost command from the signal corresponding to the difference evaluated between the set point I_{Lref} and the current in the inductor I_L. The transfer function of the controller is given by the following:

$$Cs = \frac{K_i}{S} + K \tag{10}$$

The closed-loop transfer function of the controller associated with the PV system is given by the following:

$$\frac{I_{PV}}{I^*_{PV}} = \frac{\frac{K_i + K_P S}{L}}{\frac{K_i}{L} + S^2 + S\frac{K_P + R_c}{L}} = \frac{\frac{K_i + K_P S}{L}}{\omega_i^2 + S^2 + 2S\omega_i\zeta} \tag{11}$$

where I_{PV} is the current error, and I^*_{PV} is the reference current of the PV. This allowed us to determine, by identification, the coefficients *Kp* and *Ki*:

$$K_P = 2L\omega_i\zeta - R_c \tag{12}$$

And:

$$K_i = L\omega_i^2 \tag{13}$$

To regulate the boost converter, The control law was considered:

$$L\frac{dI_L}{dt} = V_{in} - (1-d)v_c = u \tag{14}$$

$$d = \frac{-V_{in} + u}{v_c} + 1 \tag{15}$$

where *d* is the duty cycle of the converter

The PWM modulation technique was then used to generate the trigger pulses to control the converter switch. The control scheme is given in Figure 4.
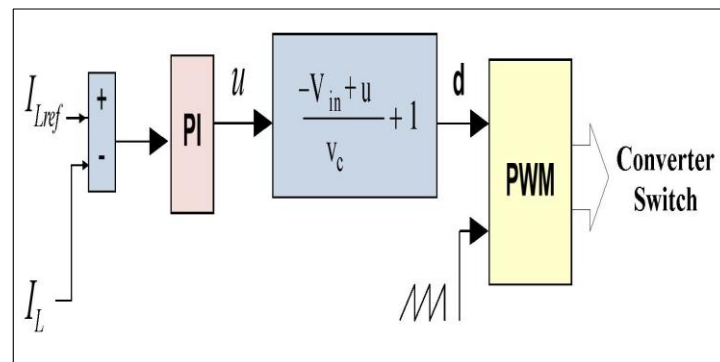
Figure 4. The control scheme of a boost converter.

To validate the results, Matlab simulation software was used to test the behavior of the photovoltaic system connected to the power grid. The disturbances were added to the system with variations of loads, solar radiation, and the rate of charge and discharge of the battery. Figure 5 shows the proposed diagram of PV connected to the grid.

3.1. Nonlinear Control Technique of an Inverter

The inverter was placed downstream from the boost converter and upstream from the grid. Its principal function is to deliver the alternating currents and voltages from a DC power source. A nonlinear control technique was used to compensate for the harmonic currents generated by the nonlinear load, maintain the imbalance load, regulate the DC bus voltage, and compensate for the reactive power consumed by the load. Reactive power compensation is a technique used to manage and mitigate the reactive power in an electrical system. The range of power factor (cos φ) within which reactive power compensation can be achieved depends on the design and capabilities of the controller. In general, a controller such as SVC or STATCOM can operate over a wide range of power factors, typically ranging from lagging (inductive loads) to leading (capacitive loads). The control algorithm employed in these controllers is often based on voltage or current measurement

feedback and utilizes closed-loop control techniques. The controller monitors the system voltage and current and adjusts the reactive power output accordingly to maintain a desired power factor or to compensate for reactive power fluctuations. A model of the active filter using these differential equations (park transformation) that passes from the '*abc*' plane to the '*dq*' plane.
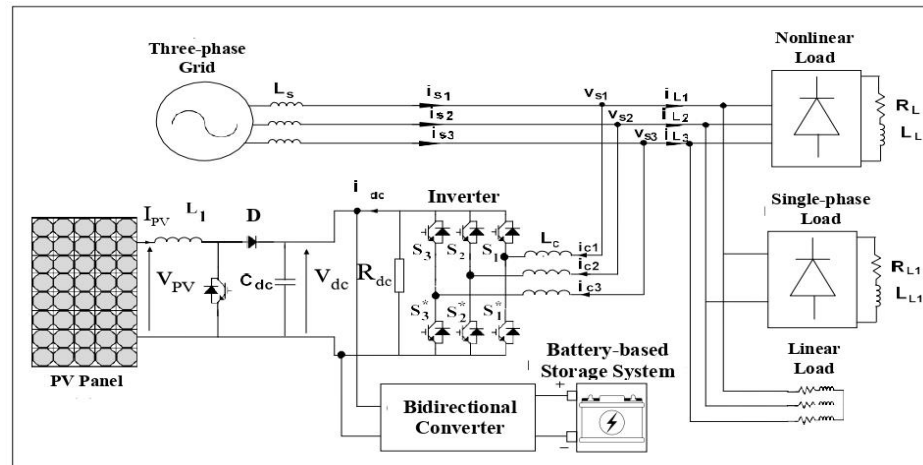

Figure 5. Proposed diagram of PV connected grid.

3.1.1. Modeling the '*abc*' Plane Transformation

At first, we used Kirchhoff's laws for each phase of the connection point of the inverter: The equations can be written as:

$$\begin{cases} v_1 = V_{MN} + V_{1M} + R_C i_1 + L_C \frac{di_1}{dt} \\ v_2 = V_{MN} + V_{2M} + R_C i_2 + L_C \frac{di_2}{dt} \\ v_3 = V_{MN} + V_{3M} + R_C i_3 + L_C \frac{di_3}{dt} \end{cases} \tag{16}$$

It's assumed that the voltages are balanced here, and the zero-sequence component is zero. After simplification, the systems of equations become:

$$\begin{cases} v_1 - d_{n1} V_{DC} - R_C i_1 = L_C \frac{di_1}{dt} \\ v_2 - d_{n2} V_{DC} - R_C i_2 = L_C \frac{di_2}{dt} \\ v_3 - d_{n3} V_{DC} - R_C i_3 = L_C \frac{di_3}{dt} \end{cases} \tag{17}$$

At the DC bus terminal, we have the equality of:

$$i_{DC} = C_{DC} \frac{dV_{DC}}{dt} \tag{18}$$

Now we give the state representation of the active filter in the plane of '*abc*' in the current system without taking into account the absence of the zero-sequence component:

$$\begin{cases} v_1 - d_{n1} V_{DC} - R_C i_1 = L_C \frac{di_1}{dt} \\ v_2 - d_{n2} V_{DC} - R_C i_2 = L_C \frac{di_2}{dt} \\ i_1 (d_{n2} + 2d_{n1}) \frac{1}{C_{DC}} = \frac{dV_{DC}}{dt} \end{cases} \tag{19}$$

The active filters help reduce THD source current and are linked to the inverter to maintain the grid control strategies. Two control strategies of the inverter (voltage source active filter) are studied here.

3.1.2. Modeling the Filter '*abc/dq*' Plane Transformation

The filter model *d-q* stationary plane is transformed to accelerate the implementation and reduce the computation time. By using Equations (18) and (19) the model gives a relation in the following form:

$$C_{DC}\frac{dV_{DC}}{dt} = d_{n1}i_1 + d_{n2}i_2 + d_{n3}i_3 = [d_{n1} + d_{n2} + d_{n3}]\begin{bmatrix}i_1\\i_2\\i_3\end{bmatrix} \tag{20}$$

Based on Equation (20), the transition performs from the '*abc*' plane to the '*dq0*' plane.

$$C_{dq}^{123}f_{dq0} = f_{123} \tag{21}$$

$$C_{dq}^{123} = \sqrt{\frac{2}{3}\begin{bmatrix} Cos\theta & Cos\left(\theta - \frac{2\pi}{3}\right) & Cos\left(\theta - \frac{4\pi}{3}\right) \\ -Sin\theta & -Sin\left(\theta - \frac{2\pi}{3}\right) & Sin\left(\theta - \frac{4\pi}{3}\right) \end{bmatrix}} \tag{22}$$

$$\frac{dV_{DC}}{dt} = \frac{d_{nd}i_d}{C_{DC}} + \frac{d_{nq}i_q}{C_{DC}} + \frac{d_{n0}i_0}{C_{DC}} \tag{23}$$

Without taking the zero sequence components into account:

$$\frac{dV_{DC}}{dt} = \frac{d_{nd}i_d}{C_{DC}} + \frac{d_{nq}i_q}{C_{DC}} \tag{24}$$

$$L_C\frac{di_d}{dt} = V_d - R_Ci_d + L_C\omega i_d - d_{nd}V_{DC} \tag{25}$$

$$L_C\frac{di_q}{dt} = V_q - R_Ci_q - L_C\omega i_q - d_{nq}V_{DC} \tag{26}$$

$$C_{DC}\frac{dV_{DC}}{dt} = d_{nd}i_d + d_{nq}i_q \tag{27}$$

In order to carry out a good follow-up of the instructions, we must have current loops on the axes of *d* and *q* that are relatively fast. The first two differential equations of the model (18) are established and can be rewritten in the following form:

$$u_d = R_Ci_d + L_C\frac{di_d}{dt} = V_d + L_C\omega i_q - d_{nd}V_{DC} \tag{28}$$

$$u_q = R_Ci_q + L_C\frac{di_q}{dt} = V_q - L_C\omega i_d - d_{nq}V_{DC} \tag{29}$$

These equations represent the dynamics of the active filter's nonlinear current of *id*, and *iq*. The currents *id* and *iq* can be controlled independently by inputs u_d and u_q. The Proportional-Integrator controllers are used for rapid dynamic response to canceling the steady-state error. PI controllers have the following expressions:

$$u_d = \tilde{I}_d K_p + K_i \int \tilde{I}_d \, dt \tag{30}$$

$$u_q = \tilde{I}_q K_p + K_i \int \tilde{I}_q \, dt \tag{31}$$

The closed loop current transfer function is given by the following:

$$\frac{I_d(s)}{I_d^*(s)} = \frac{I_q(s)}{I_q^*(s)} = \frac{s + \frac{k_i}{k_p}}{s^2 + \frac{(R_c + k_p)}{L_c} + \frac{k_i}{L_c}} \cdot \frac{k_P}{L_c} \tag{32}$$

where $\widetilde{I_d}$ and $\widetilde{I_q}$ are represent the errors of the currents and I_d^* and I_q^* are represent the references of the currents. The current regulator parameters are as follows:

$$K_p = 2\xi L_c \omega_{ni} - R_c \text{ and } K_i = \omega_{ni}^2 L_c \tag{33}$$

where $\xi = \frac{\sqrt{2}}{2}$; ω_{ni} must be selected less than $\omega_{nis} = 2\pi f_s$; f_s is switching frequency. From Equations (28) and (29), we determined the control laws as follows:

$$d_{nd} = \frac{V_d - u_d + L_C \omega i_q}{V_{DC}} \tag{34}$$

$$d_{nq} = \frac{V_q - u_q - L_C \omega i_d}{V_{DC}} \tag{35}$$

The analysis of the voltage loop is based on Equations (25)–(27), defined as the equivalent input of

$$u_{DC} = d_{nd} i_d + d_{nq} i_q = \frac{dv_{DC}}{dt} C_{DC} \tag{36}$$

The transfer function of the regulator is written as follows:

$$G_v = \frac{U_{DC}}{\widetilde{V_{DC}}} = \frac{\frac{K_{iv}}{k_{pv}} + S}{S} \cdot k_{pv} \tag{37}$$

The closed-loop transfer function is given by the following:

$$\frac{V_{DC}(S)}{V_{DC}^*(S)} = \frac{\frac{K_{pv}S + K_{iv}}{C_{DC}}}{S^2 + \frac{(K_{pv})}{C_{DC}} \cdot S + \frac{K_{iv}}{C_{DC}}} = \frac{\frac{\omega}{2\xi} + s}{S^2 + 2\xi\omega S + \omega^2} \cdot 2\xi \tag{38}$$

where $\widetilde{V_{DC}}$ is the voltage error and V_{DC}^* is the voltage reference of V_{DC}; $k_{pv} = 2\xi\omega C_{DC}$ and $K_{iv} = \omega^2 C_{DC}$. To regulate the DC bus voltage and to compensate for the losses in the dissipative elements of the filter, an active current i_{d0} is added to the reference current i_d.

We have:

$$i_{d0} = \frac{u_{DC}V_{DC} - d_{nq}V_{DC}i_q}{d_{nd}V_{DC}} = \frac{u_{DC} - d_{nq}i_q}{d_{nd}} \tag{39}$$

$$d_{nq}V_{DC} \approx V_q = 0 \tag{40}$$

$$d_{nd}V_{DC} \approx V_q = \sqrt{\frac{2}{3}} V_{smax} \tag{41}$$

$$i_{d0} \approx u_{DC}\sqrt{\frac{2}{3}} \frac{V_{DC}}{\hat{V}} \tag{42}$$

The following transfer function has been used in the filter:

$$H(s) = \frac{s + 2s\omega\xi}{s^2 + 2s\omega\xi + \omega^2} \tag{43}$$

By plotting it to the Bode diagram for different cutoff frequencies, with f_c =15 Hz, and 65 Hz, we get the following graph:

Figure 6 shows that for a frequency greater than 60 Hz, the harmonic current will be higher than $\omega = 377$ rd/s. For a cutoff frequency $f = 15$ Hz, the modulus in dB is almost zero, demonstrating no amplitude modification between the input and the output of the high pass filter. Moreover, the phase is also zero, indicating no phase shift between the input and the output of the high-pass filter. For a cutoff frequency $f = 65$ Hz, the modulus in dB is approximately 2 dB, demonstrating a modification of amplitude between the input and the output of the high pass filter. Moreover, the phase is not zero, showing a phase difference between the input and the output of the high-pass filter. It is evident that the cutoff frequency at 15 Hz is suitable for compensating for the unbalanced load since there is no change in the input and output signal, neither in amplitude nor phase.
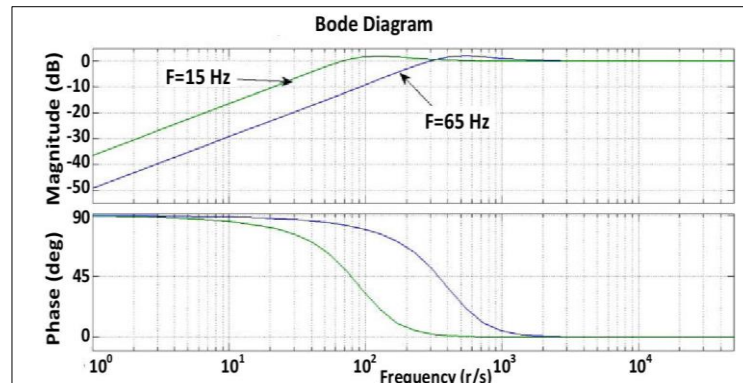
Figure 6. Bode diagram of the filter for different cutoff frequencies.

It is seen that the current of the grid is more disturbed for the higher frequency. Figure 7 shows the block diagram of the *dq* command. The currents supplied by the active filter are controlled in the *dq* plane using an equivalent control strategy based on synchronous *dq*. The harmonic references current i_{Ld} and i_{Lq} are extracted from the load currents. A PI Controller is used for the current loops (inner loops) in order to allow the filter currents to follow their references quickly. For the external loop (voltage loop), a PI controller is also used to bring the DC voltage V_{DC} back to its set value. The compensated error is added to the output of the reference current along with the *d*-axis.
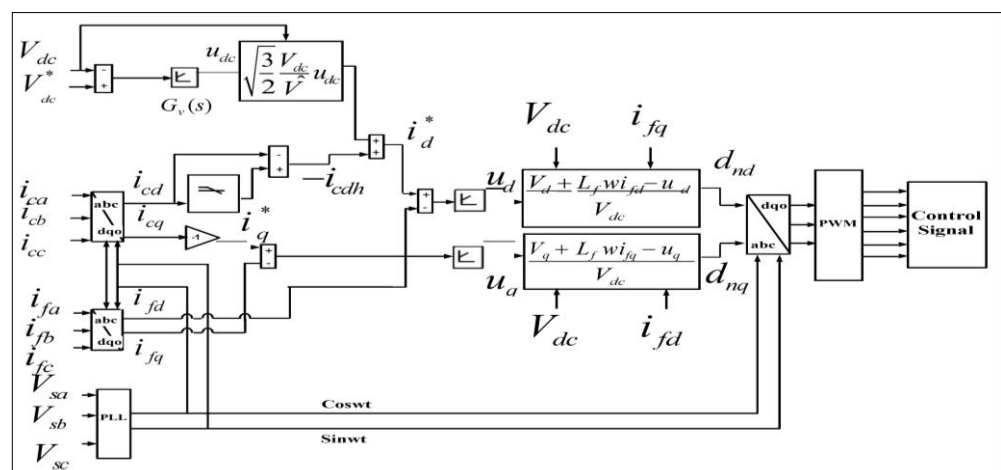
Figure 7. Block diagram of nonlinear control.

3.2. Nonlinear Control with Adaptive Notch Filter

This method is used to analyze the filter inspired by the work carried out by Karimi-Ghartemani in 2006 [37].

$$u(t) = u_1(t) + u_0(t) \tag{44}$$

$$u_0(t) = A_0 sin(d_0 + w_0 t) \tag{45}$$

The undesired signal can be assimilated to noise, transient disturbances, and sinusoidal components with a frequency different from ω_0 (center frequency). We wish to obtain an estimate of $u_0(t)$, designated by $y(t)$, from the signal $u(t)$. The least-squares error between the input signal $u(t)$ and output $y(t)$ is minimized by a method called gradient descent. It is the starting point for various adaptive algorithms, such as the linear least squares method. The cost function is defined by:

$$J(t, Q) = \frac{1}{2}[u(t) - y(t, Q)]^2 = \frac{1}{2}e^2(t, Q) \tag{46}$$

The system comprises a conventional phase-locked loop associated with an amplitude estimator and an adjustment unit. The dynamic system receives the input signal $u(t)$ and provides a real-time estimate of the fundamental component $y(t)$, the amplitude $V(t)$ of $y(t)$, the frequency and the phase $\Delta\omega(t) = \omega(t) - \omega_0$ and the phase $\varphi(t)$ of $y(t)$. The estimated time derivative of the amplitude, phase, and frequency is then estimated. The error signal $e(t) = u(t) - y(\text{t})$ is the input distortion signal. The speed and accuracy of the response are determined by the parameters of k_1, k_2, and k_3. It controls the behavior of the response both at the transient level and at the steady state. This system has the ability to be inherently adaptive and follows variations in amplitude, phase angle, and frequency of the input signal. It can provide an accurate estimate of the fundamental component of the polluted signal. Its simple structure makes this notch filter suitable for real-time applications. Therefore, the derivatives of A, ω, and φ can be formulated by the equations.

$$\begin{cases} \dot{A}(t) = k_1 e(t) sin\varphi(t) \\ \dot{\omega}(t) = k_2 e(t) cos\varphi(t) \\ \dot{\varphi}(t) = \omega(t) + k_2 k_3 e(t) cos\varphi(t) \\ y(t) = A(t) sin\varphi(t) \end{cases} \tag{47}$$

The block diagram of the Adaptive Notch Filter is shown in Figure 8.
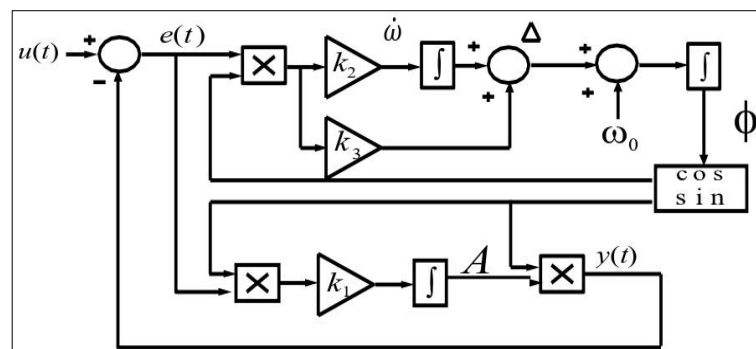
Figure 8. The operational block diagram of the adaptive notch filter.

Therefore, we integrated this filter into the simple nonlinear control proposed by using it as an input signal of load currents. Our simulations show that the inverter control does not adequately compensate for the currents. Hence we need to introduce the inverse component in a control system to correct this imperfection. We will therefore capture the input currents and perform an inverse transformation before injecting them at the output. The equation governs the negative sequence component of the load current.

$$I_{inv} = L_{La} + aL_{Lc} + a^2 L_{Lb} \tag{48}$$

By integrating it into the global diagram of the filter, we obtain the final diagram of the modified Adaptive Notch Filter shown in Figure 9.
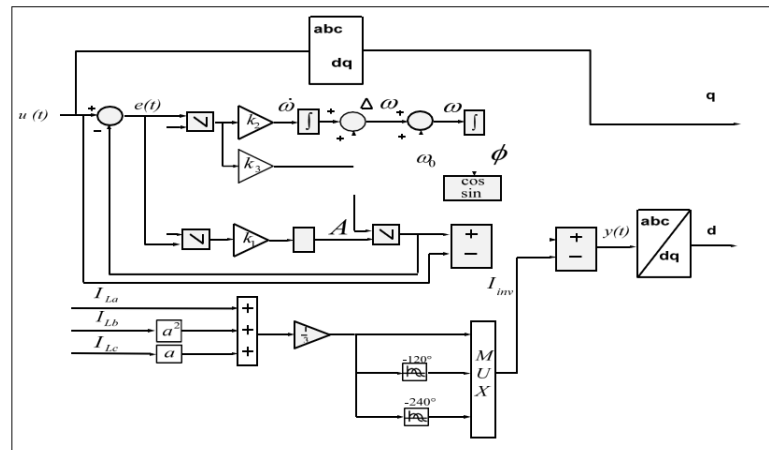
Figure 9. Final diagram of the modified Adaptive Notch Filter.

3.3. Nonlinear Control with Multi-Variable Filter

The main objective of this control strategy is to improve the performance of the nonlinear control by using a multi-variable filter. This filter can directly extract the direct fundamental component of input signals in a voltage or current, along with the *dq* axes. It can also isolate a harmonic in a particular order (direct or inverse). The following equation expresses a method to recover the transfer function from integrating the synchronous reference signal [38].

$$x_{\alpha\beta}(t) = e^{jwt} \int V_{xy}(t)\, e^{-jwt} dt \tag{49}$$

$$H(s) = \frac{x_{\alpha\beta}(s)}{\hat{x}_{\alpha\beta}(s)} = \frac{s + \omega j}{s^2 + \omega^2} \tag{50}$$

This transfer function makes it possible to demonstrate the input signal in phase with the output signal. Integrating the signal amplitude with the input signal affects its magnitude. We add two constants k_1 and k_2, to the previous transfer function to obtain the following equation:

$$H(s) = \frac{x_{\alpha\beta}(s)}{\hat{x}_{\alpha\beta}(s)} = \frac{(k_1 + s) + \omega_c j}{(k_1 + s)^2 + \omega_c^2} \cdot k_2 \tag{51}$$

To obtain $H(s) = 0$ dB, we must take $K = k_1 = k_2$. Therefore, the Laplace transforms transfer function of the multi-variable filter *H(s)* becomes:

$$H(s) = \frac{x_{\alpha\beta}(s)}{\hat{x}_{\alpha\beta}(s)} = \frac{(K + s) + \omega_c j}{(K + s)^2 + \omega_c^2} \cdot K \tag{52}$$

where K is a positive constant, $x_{\alpha\beta}$ is an input signal, and $\hat{x}_{\alpha\beta}$ is an output signal of the multi-variable filter. We draw the Bode diagram of the transfer function directly from Simulink using 'linear control design' for three values for $K = 1500$, 15,000, and 150,000, shown in Figure 10.
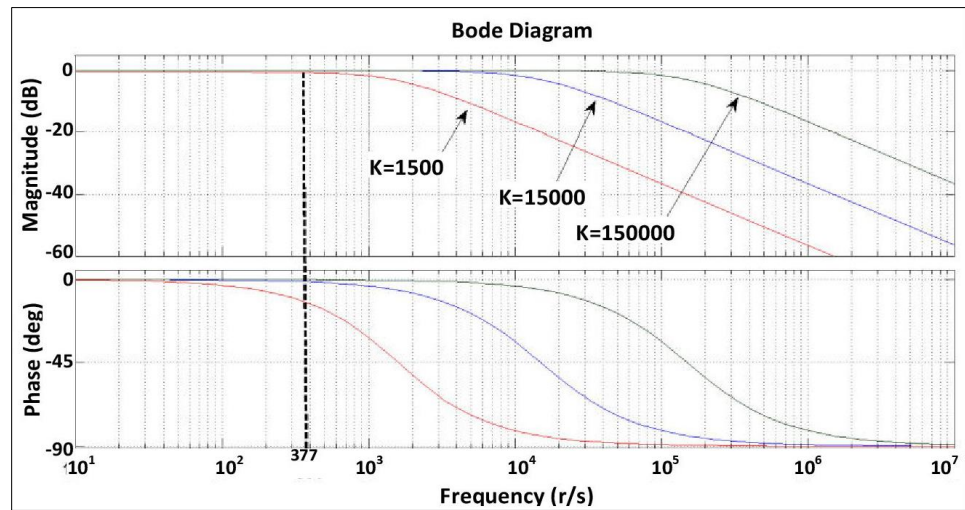
Figure 10. Bode diagram representation of different values of K.

We are looking for the value of *K*, which gives us a zero phase shift and dB modulus at the frequency of the electrical grid, *f* = 60 Hz or *ω* = 377 rd/s. The values retained are those greater than 15,000. The amplitude remains high for a higher value of *K*, and the phase remains equal to zero. Figure 11 shows the Total Harmonic Distortion (THD) of the grid for different values of *K* in the transfer function.
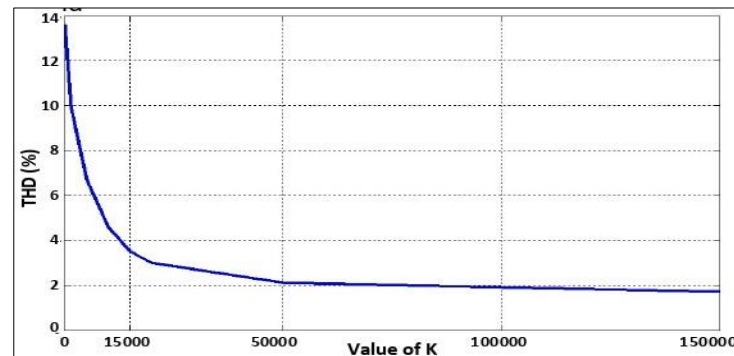

Figure 11. THD of the grid for different values of K.

We can conclude from this figure that when we increase the value of *K*, the rate of harmonic distortion in the grid is reduced. The THD of the grid remains below 5% when the value of *K* is increased from *K* = 10,000. Thus, by using a multi-variable filter, the direct or inverse fundamental and harmonic components of the input signals (voltage or current) can be extracted directly along the *dq* axes without phase shift or amplitude change. From the transfer function, we obtain the following equations.

$$\hat{x}_\alpha(s) = x_\alpha(s)\frac{(K+s)\cdot K}{(K+s)^2 + \omega_c^2} - x_\beta(s)\frac{\omega_c K}{(K+s)^2 + \omega_c^2} \tag{53}$$

$$\hat{x}_\beta(s) = x_\alpha(s)\frac{\omega_c K}{(K+s)^2 + \omega_c^2} + \frac{(K+s)\cdot K}{(K+s)^2 + \omega_c^2}\, x_\beta(s) \tag{54}$$

$$\hat{x}_\alpha(s) = [x_\alpha(s) - \hat{x}_\alpha(s)]\frac{K}{s} - \hat{x}_\beta(s)\cdot\frac{\omega_c}{s} \tag{55}$$

$$\hat{x}_\beta(s) = [x_\beta(s) - \hat{x}_\beta(s)]\frac{K}{s} + \hat{x}_a(s)\cdot\frac{\omega_c}{s} \tag{56}$$

Therefore, we integrated this filter into the proposed nonlinear controller by using it as input signals of the load currents of the grid.

3.4. Nonlinear Control without Filter

A simple nonlinear control is proposed to extract the grid's current harmonics to avoid using a traditional high-pass filter. This control is based on using the positive sequence of the load current. The inverter has the ability to compensate for all undesired current harmonics, unbalanced load currents, and reactive power consumed by the loads [39].

$$L_c \omega i_{cq} - d_{nd} v_{dc} + v_d = L_c \frac{di_{cd}}{dt} \tag{57}$$

$$-L_c \omega i_{cd} - d_{nq} v_{dc} + v_q = L_c \frac{di_{cq}}{dt} \tag{58}$$

$$d_{nd} i_{cd} + d_{nd} i_{cq} = C_{dc} \frac{dv_{dc}}{dt} + \frac{v_{dc}}{R_{dc}} \tag{59}$$

$$L_c \frac{di_{Ld}}{dt} - L_c \omega i_{Lq} + L_c \omega i_{sq} - d_{nd} v_{dc} + v_d = L_c \frac{di_{sd}}{dt}$$
$$L_c \frac{di_{Lq}}{dt} + L_c \omega i_{Ld} - L_c \omega i_{sd} - d_{nq} v_{dc} + v_q = L_c \frac{di_q}{dt} \tag{60}$$

To maintain V_{dc} equal to its reference, the DC bus voltage regulator uses a proportional-integral PI as an output component i_{d0} to maintain the DC bus voltage and reduce the losses in the converter.

$$i_{d0} = \frac{v_{dc} u_{dc}}{v_{dc} d_{nd}} = \frac{u_{dc}}{d_{nd}} = \sqrt{\frac{2}{3}} u_{dc} \frac{v_{dc}}{\hat{V}} \tag{61}$$

$$d_{nd} = \frac{L_c \frac{di_{Ld}}{dt} - L_c \omega i_{Lq} + L_c \omega i_{sq} - d_{nd} v_{dc} + v_d - u_d}{v_{dc}} \tag{62}$$

$$d_{nq} = \frac{L_c \frac{di_{Lq}}{dt} + L_c \omega i_{Ld} - L_c \omega i_{sd} - d_{nq} v_{dc} + v_q - u_q}{v_{dc}} \tag{63}$$

The diagram of the nonlinear controller without an inverter filter is shown in Figure 12.
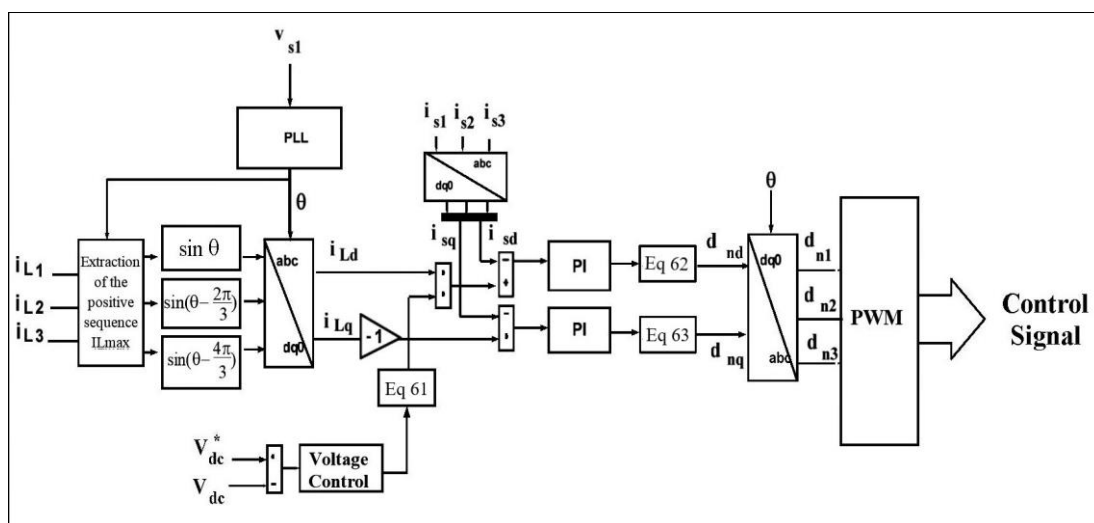
Figure 12. Diagram of the nonlinear controller without an inverter filter.

The following values will be used for the simulation of the grid as shown in Table 1:

Table 1. Simulation data of the proposed grid.

Sources	Symbols/Parameters
Solar Panel	Radiation 800 W/m^2, Current I$_{PV}$ = 40 A, Voltage V$_{PV}$ = 150 V, Power P$_{PV}$ = 6000 W;
Bidirectional Converter	nductance L = 5 mH, Capacitance C = 200·10^{-6} F
Loads	Nonlinear load R$_L$ = 30 Ω, L$_L$ = 10 mH; Single-phase load: R$_{L1}$ = 50 Ω, L$_{L1}$ = 10 mH; Linear load R$_{L2}$ = 30 Ω, L$_{L2}$ = 10 mH
Inverter/Rectifier	Lc = 5 mH, Ls = 0.5 mH
Three-Phase Grid	Frequency 60 Hz and a Voltage phase 208 V
Storage System	Li-ion- 20 Ah, SOC 70%

4. Simulation Results

4.1. Using a Simple Nonlinear Controller

4.1.1. Assembled with Loads, Solar Radiation, and without a Battery System

Using Matlab/Simulink software, we analyzed a system consisting of a photovoltaic panel connected to the three-phase grid with an unbalanced nonlinear load. At t = 0.1 s, solar radiation is fixed at G = 800 W/m^2. We obtained the powers, currents, and voltage curves at a certain point level to understand the effect of each subsystem of the entire grid. The THD rate of the grid and loads are also considered here. Figures 13 and 14 show the dynamic response of the grid and power flow in the grid with solar radiation of G = 800 W/m^2 without a storage system. Figure 15 shows the harmonic spectrum of the grids and load current.
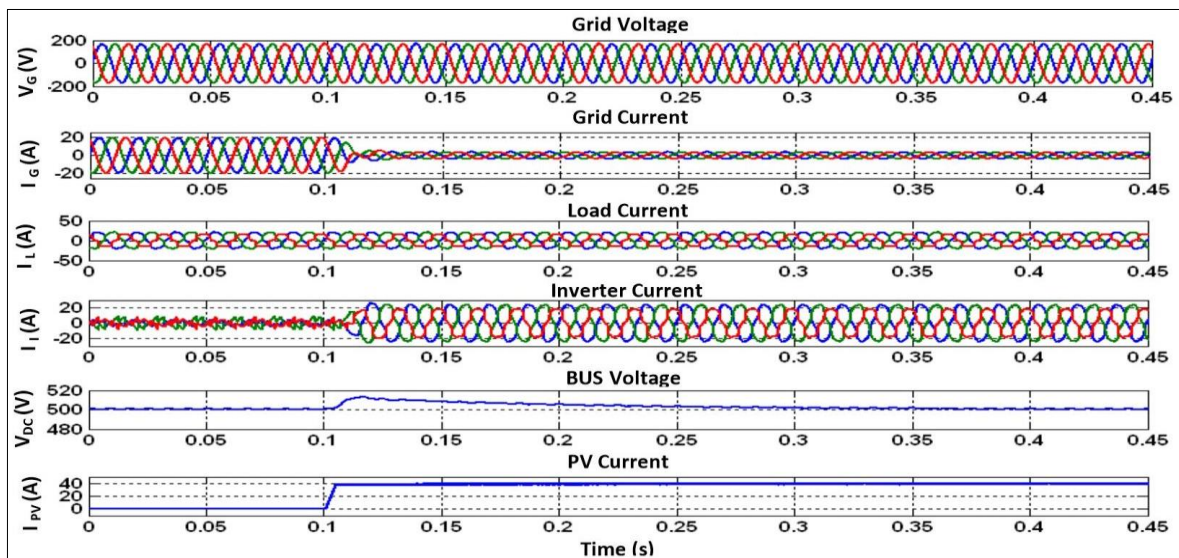
Figure 13. Dynamic response of the grid with solar radiation of G = 800 W/m^2.

From the above simulation, we analyzed that the grid's current is in phase with the voltage. As a result, the current provides a part of the power to the battery and loads. In the presence of solar radiation, the current is out of phase with the voltage. Therefore it receives power. The V_{dc} is adequately regulated here. With G = 800 W/m^2, we observe a current of 40 A generated by the solar panel. The power curves confirm that the load is supplied at 5000 W at first entirely by the grid, then the solar panel provides 6000 W under sunny conditions. At the same time, it can also feed the grid up to 1000 W. We also observed a grid THD of 0.93%.
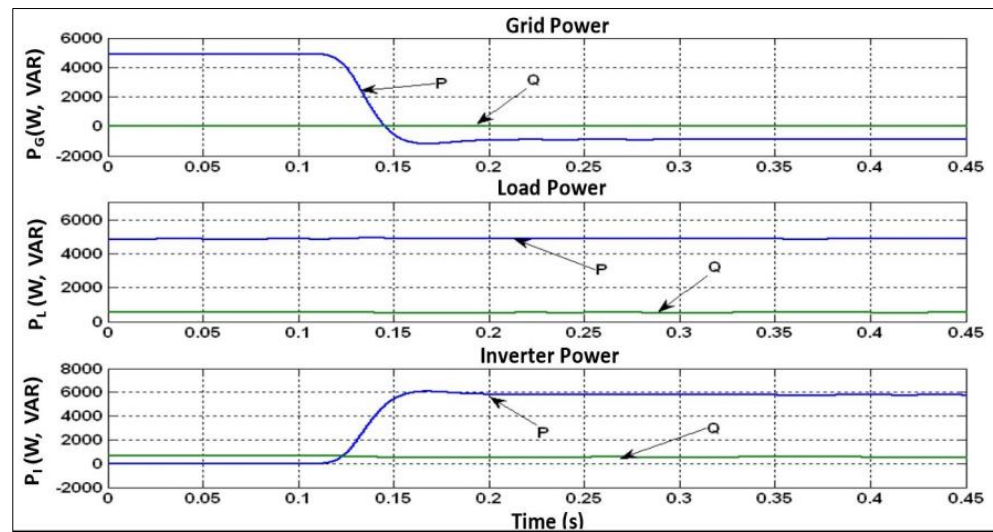
Figure 14. Power flow in the grid with solar radiation $G = 800 \text{W}/\text{m}^2$.
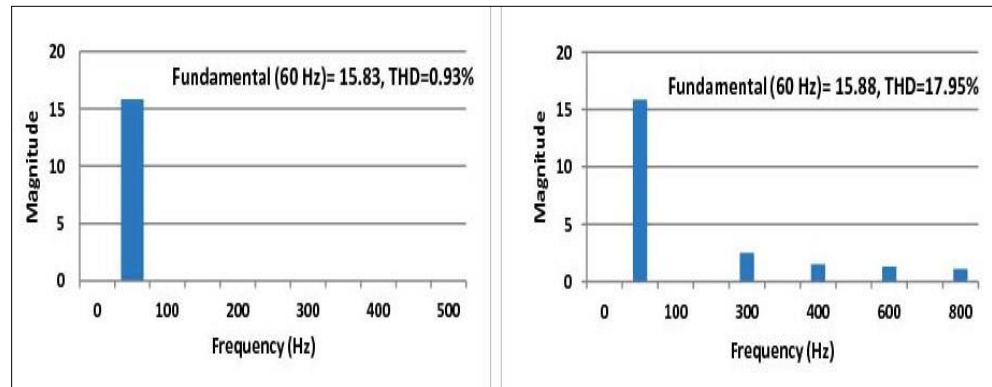

Figure 15. Harmonic spectrum of the grids and load current with solar radiation of $G = 800 \text{ W}/\text{m}^2$.

4.1.2. Assembled with Load, Solar Radiation, and Variation of the Battery Charge

For this simulation, we use the same assembly as before to allow the storage system to compensate for the variations of power generated by the solar panel due to climatic conditions. At $t = 0$ s, the solar radiation is fixed at $G = 800 \text{ W}/\text{m}^2$. On the other hand, the current of the battery is varied. Indeed, through the control of the DC-DC converter, we imposed a current to charge battery $I_{in} = 20$ A from $t = 0$ to $t = 0.1$ s, then discharged from $t = 0.1$ to 0.3 s with $I_{in} = -20$ A, and again charged from $t = 0.3$ s with $I_{in} = 20$ A. The current, voltage, and power curves are observed in Figures 16 and 17, respectively. The simulation results we obtained are shown as follows.

The current in the inverter increases at t = 0.1 to 0.3 s because of the battery discharges shown in Figure 18. The results show phase opposition between the current and the grid voltage, indicating that the grid receives power. Power curves confirmed that the inverter is negative when the battery absorbs current and positive when the battery discharges the current. The DC bus voltage is regulated here, and the current in the solar panel is constant at 40 A. The power supplied to the load is up to 5000 W. The curves relating to the battery indicate when the current imposed is negative, the battery is charged. When it is positive, it is discharged. The voltage decreases when the current increases and vice versa.
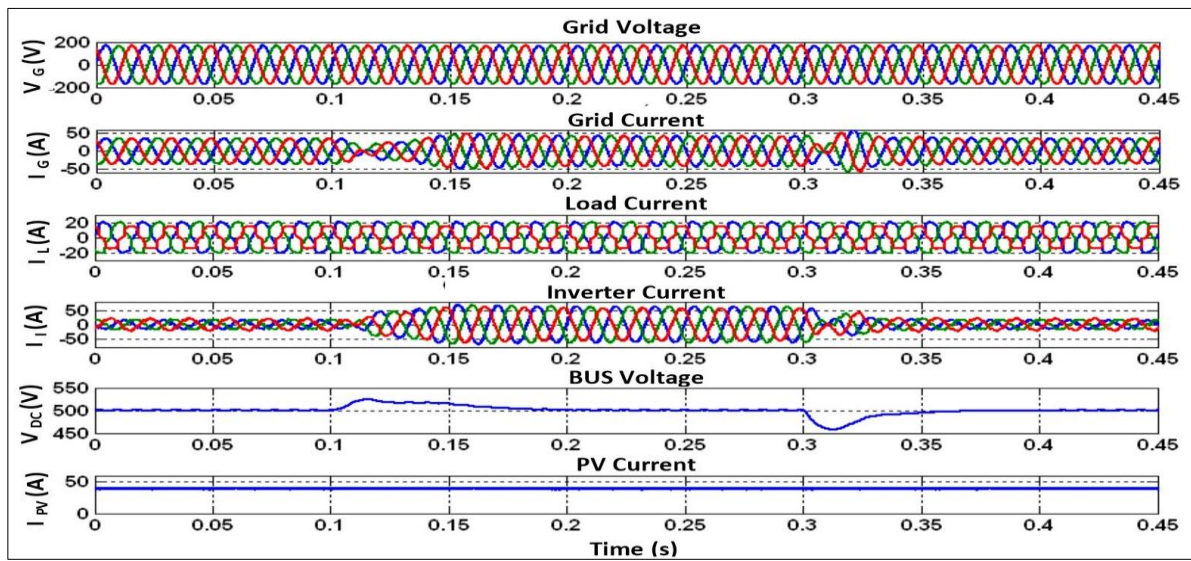
Figure 16. Dynamic state response with battery charge variation.
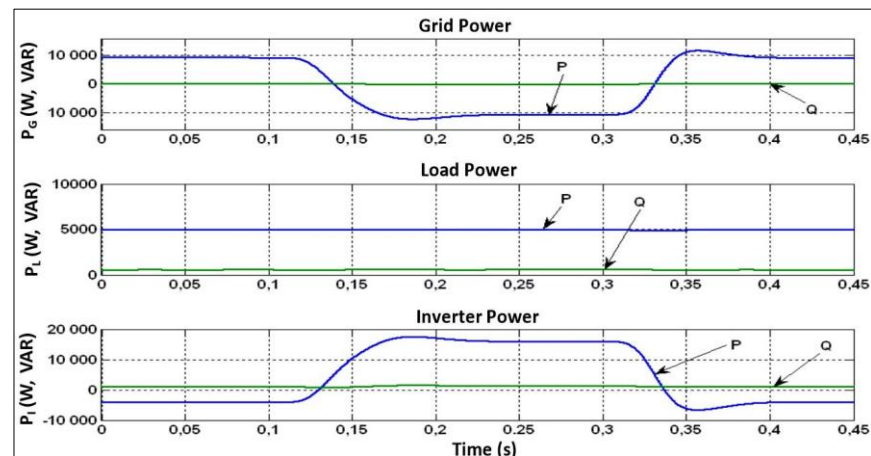
Figure 17. Power flow with battery charge variation.
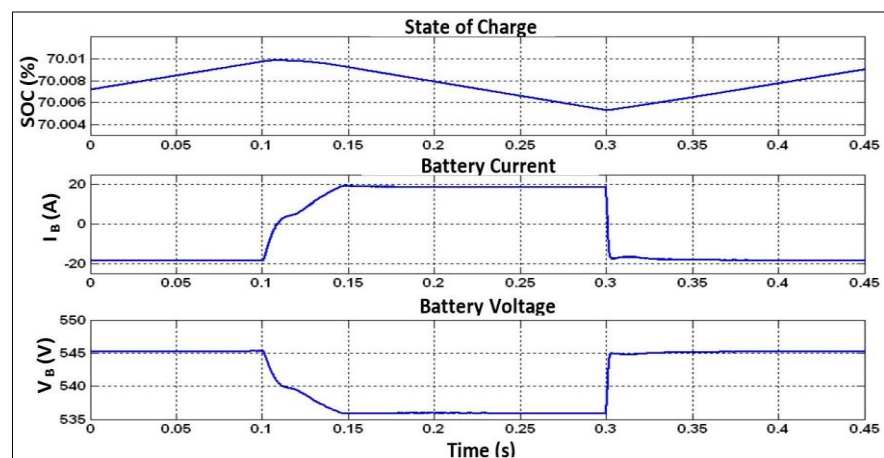
Figure 18. Battery state of charge.

4.1.3. Assembled with Solar Radiation, Battery Charge, and Variation of the Load

For this simulation, we use the same setup as the second simulation, except for the varied unbalanced load. The purpose of this operation is to analyze the assembled grid reaction to this modification. We can imagine a city as a load that needs to be supplied and requires more or less energy. The system must adapt to these variations. At $t = 0$ s, the solar radiation is set at $G = 800$ W/m^2. Between $t = 0.1$ and 0.2 s, we increase the load. At $t = 0.3$ s, we fix the load as at $t = 0$ s. The other parameters (radiation, battery charge) are constant. The same current, voltage, and power curves are observed in Figures 19 and 20 respectively, as in the first simulation. Here are the results we obtained from the simulation.
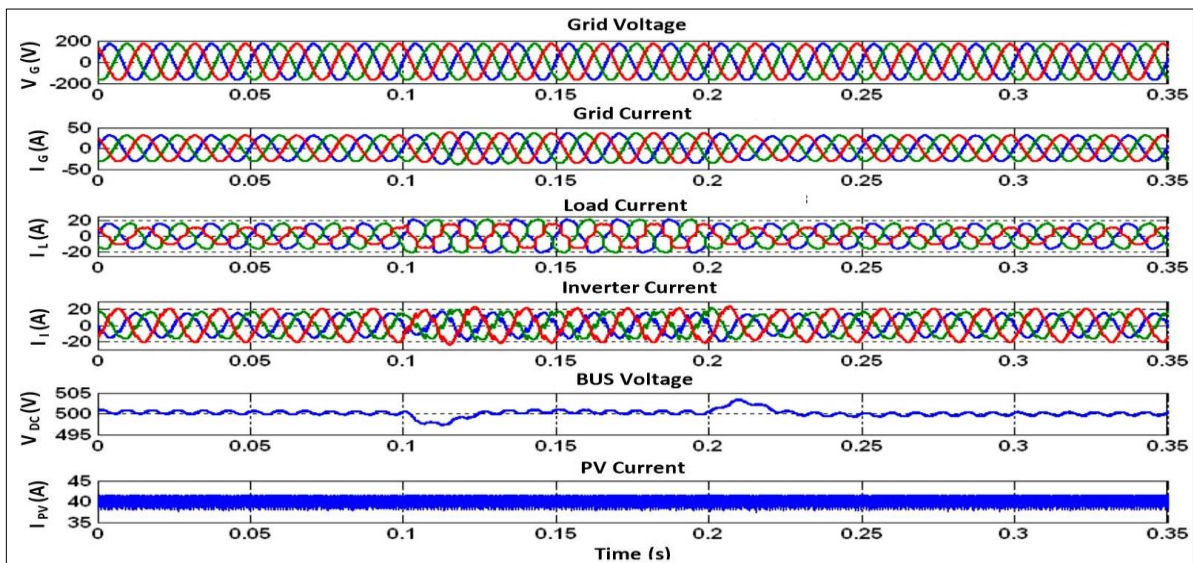
Figure 19. Dynamic response with load variation.
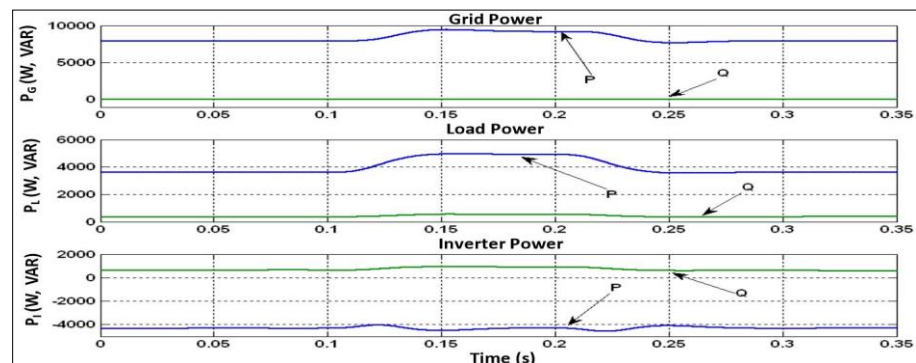
Figure 20. Power flow with load variation.

From the above-shown power curve, we observed the PV and grid that supply power to the load. When the load power increases at $t = 0.1$ s, the current in the grid increases due to the power of the grid. With solar radiation of $G = 800$ W/m^2, the PV can't support the grid to supply power to the load.

4.1.4. Assembled with Battery Charge, Load, and with Variation of the Solar Radiation

For this simulation, we used the same setup as the second simulation, except the varied solar radiation at $t = 0$ s, $G = 600$ W/m^2, at $t = 0.1$ s, $G = 800$ W/m^2, and at $t = 0.3$ s, $G = 1000$ W/m^2. The other parameters (load, battery charge) are constant. The same current, voltage, and power curves are observed in Figures 21 and 22, respectively, as in the first simulation. The simulation results we obtained are shown as follows.:
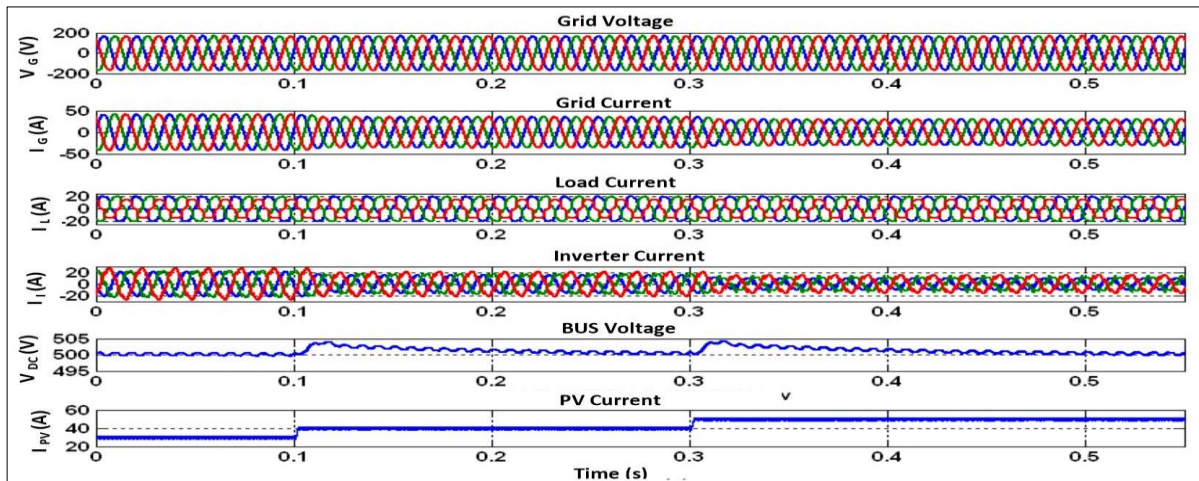
Figure 21. Dynamic response with the variation of solar radiation.
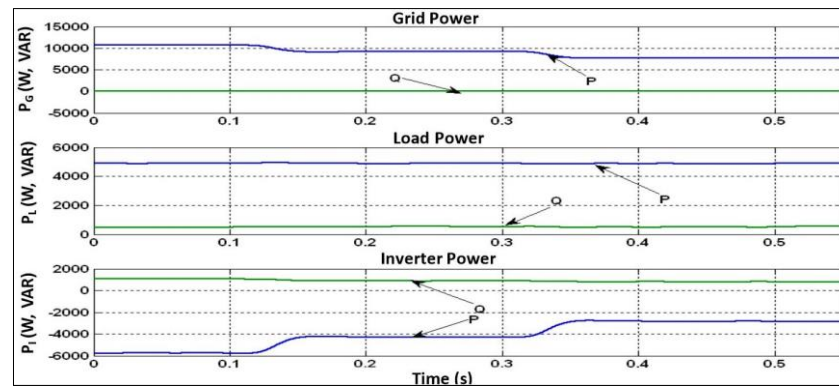

Figure 22. Power flow with a variation of solar radiation.

This simulation shows that the grid current decreases when solar radiation increases. This increment in solar radiation causes to increase in PV current from 25 A to 40 A and finally to 50 A. From the above power curve, we observed the grid power decreases, inverter power increases and the load becomes constant.

4.2. Using Nonlinear Controller with Multi-Variable Filter

4.2.1. Assembled with Loads, Solar Radiation, and without a Battery System

The same simulation is carried out as in Section 4.1.1 by replacing the simple nonlinear controller of the inverter with the nonlinear controller with a multi-variable filter. Here are the results we obtained:

We analyzed from Figure 23 that the grid current significantly decreased when solar radiation increased. In the absence of solar radiation, the current is in phase with the voltage. Therefore it supplies current. On the other side, the current is out of phase with the voltage with solar radiation. Thus it receives current. The V_{dc} is adequately regulated here. With $G = 800$ W/m^2, we observe a current of 40 A generated by the solar panel. Figure 24 shows that the power curves confirm that the load is supplied at 5000 W entirely by the grid, then the solar panel provides 6000 W under sunny conditions. At the same time, it can also feed the grid up to 1000 W. We also observed from Figure 25 that a grid THD of 1.20% is a steady-state condition.
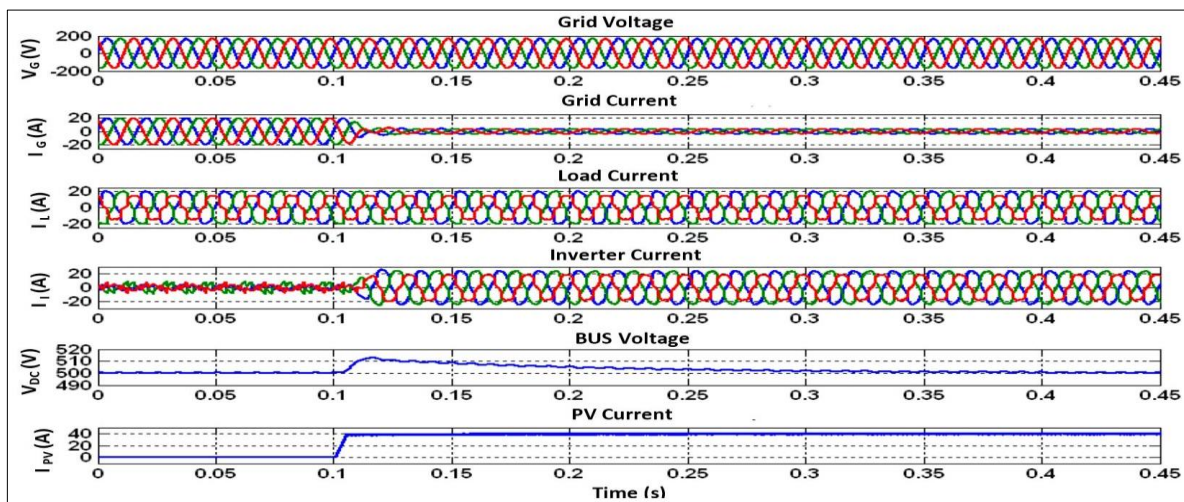
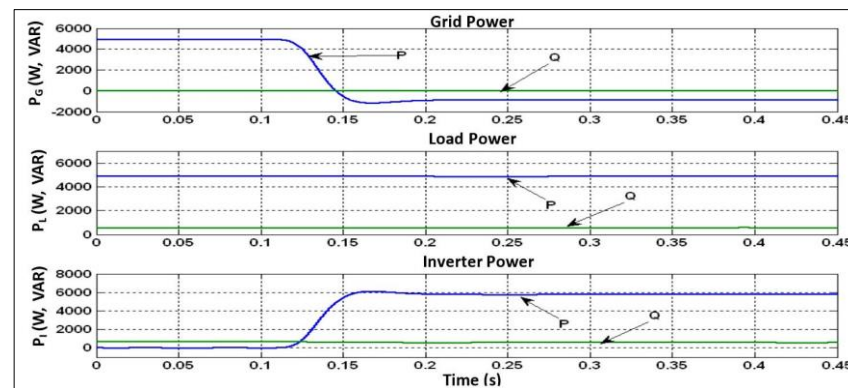**Figure 23.** Dynamic response with solar radiation of $G = 800$ W/m^2 using a multi-variable filter.

Figure 24. Power flow with the variation of solar radiation $G = 800$W/m^2 using multi-variable filter.
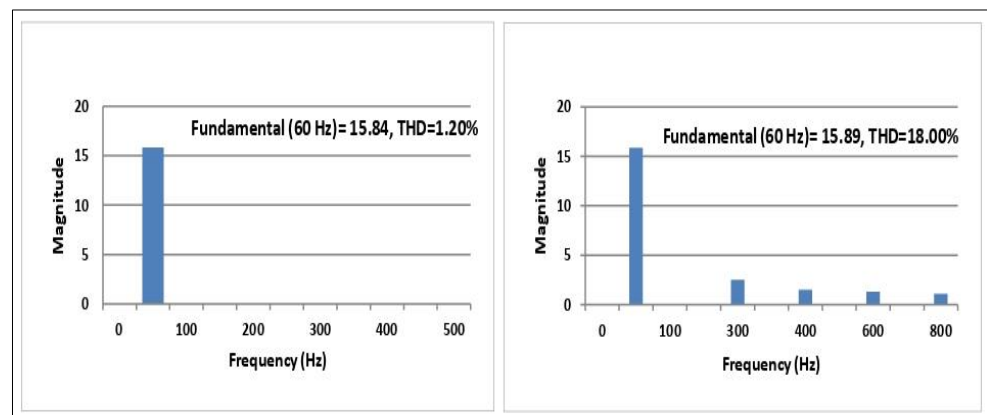

Figure 25. Harmonic spectrum of the grid and load current using a multi-variable filter.

4.2.2. Assembled with Loads, Solar Radiation, and Variations of the Battery Charge

The same simulation is carried out as in Section 4.1.2 by replacing the simple nonlinear controller of the inverter with the nonlinear controller with a multi-variable filter. Here are the results we obtained:

Figure 26 shows the current in the inverter increases at $t = 0.1$ to 0.3 s because of the battery discharges. The results show phase opposition between the current and the grid voltage, indicating that the grid receives power. Figure 27 shows the power curves confirming that the inverter is negative when the battery absorbs current and positive when

the battery discharges the current shown in Figure 28. The DC bus voltage is regulated here, and the current in the solar panel is constant at 40 A. The power supplied to the load is up to 5000 W. The curves relating to the battery indicate when the current imposed is negative, the battery is charged. When it is positive, it is discharged. The voltage decreases when the current increases and vice versa.
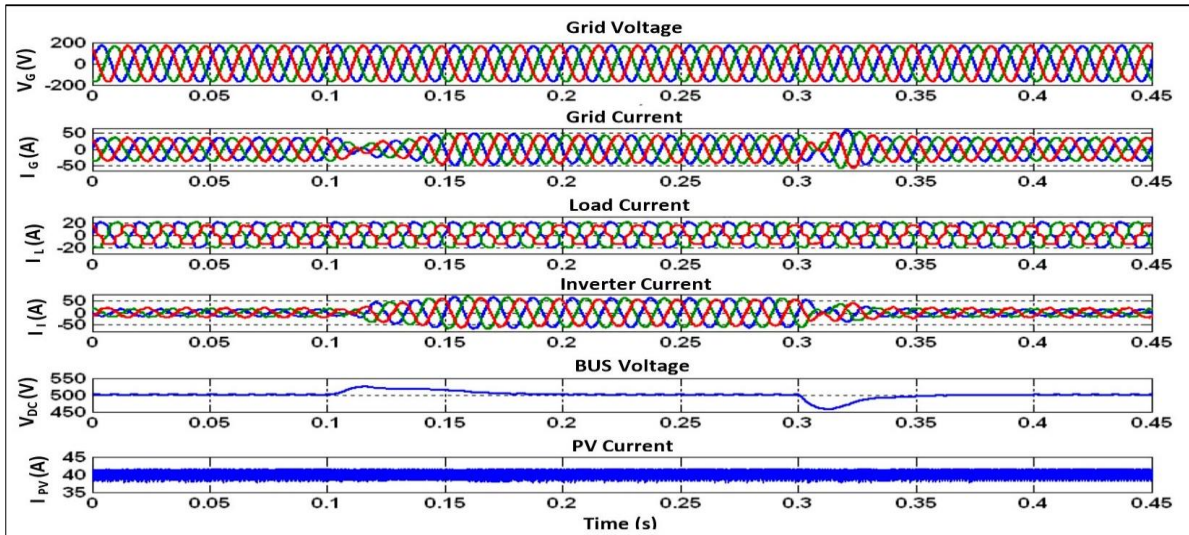

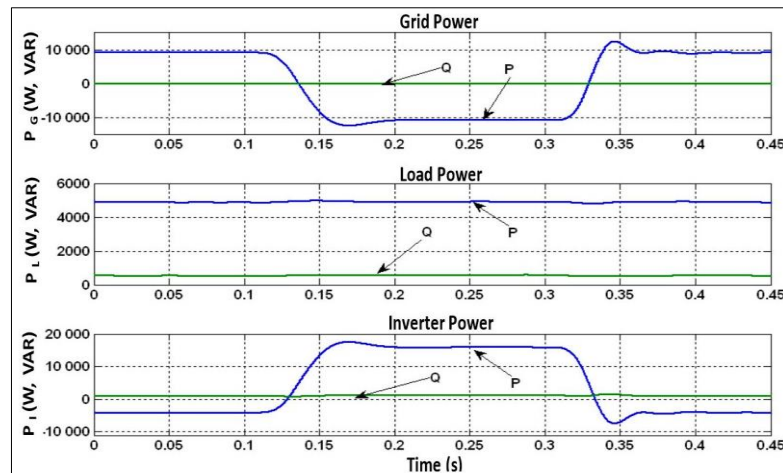**Figure 26.** Dynamic response with battery charge variation using a multi-variable filter.

Figure 27. Power flow with battery charge variation using a multi-variable filter.
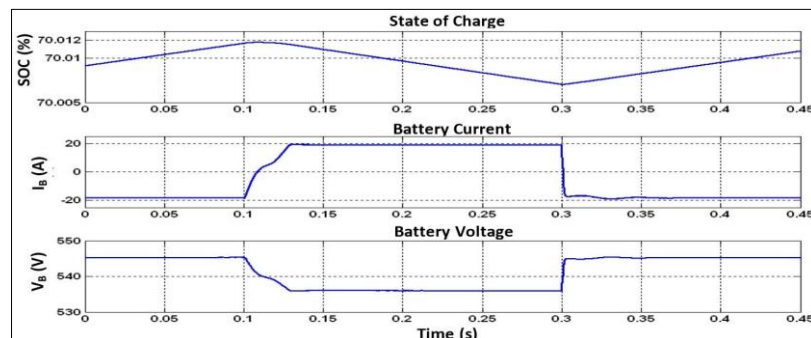
Figure 28. Battery state of charge using multi-variable filter.

4.2.3. Assembled with Solar Radiation, Battery Charge, and Variation of the Loads

The same simulation is carried out as in Section 4.1.3 by replacing the simple nonlinear controller of the inverter with the nonlinear controller with a multi-variable filter. Here are the results we obtained.

From the above power curve, we observed the PV and grid that supply power to the load. Figures 29 and 30 show when the load power increases at *t* = 0.1 s, the current in the grid increases due to the power of the grid. With the solar radiation of *G* = 800 W/m², the PV can't support the grid to supply power to the load.
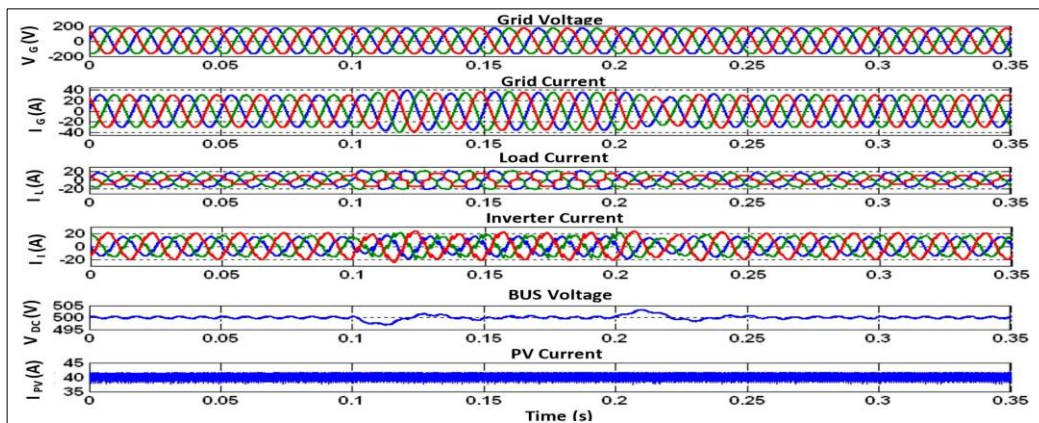
Figure 29. Dynamic response with load variation using a multi-variable filter.
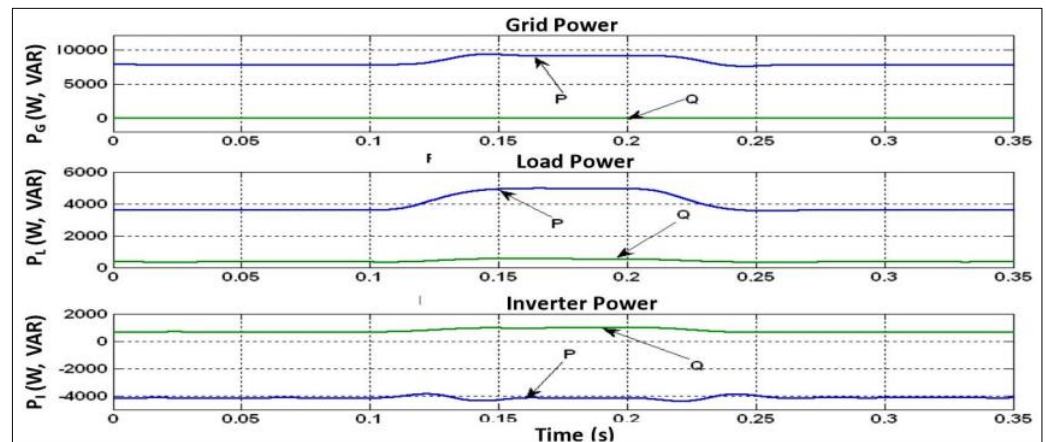
Figure 30. Power flow with a load variation multi-variable filter.

4.2.4. Assembled with Battery Charge, Load, and Variation of the Solar Radiation

The same simulation is carried out as in Section 4.1.4 by replacing the simple nonlinear controller of the inverter with the nonlinear controller with a multi-variable filter. Here are the results we obtained.

This simulation shows that the grid current decreases when solar radiation increases. This increment in solar radiation causes to increase in PV current from 25 A to 40 A and finally to 50 A shown in Figure 31. From the above power curve, we observed that the grid power decreases, inverter power increases and the load becomes constant, as shown in Figure 32.
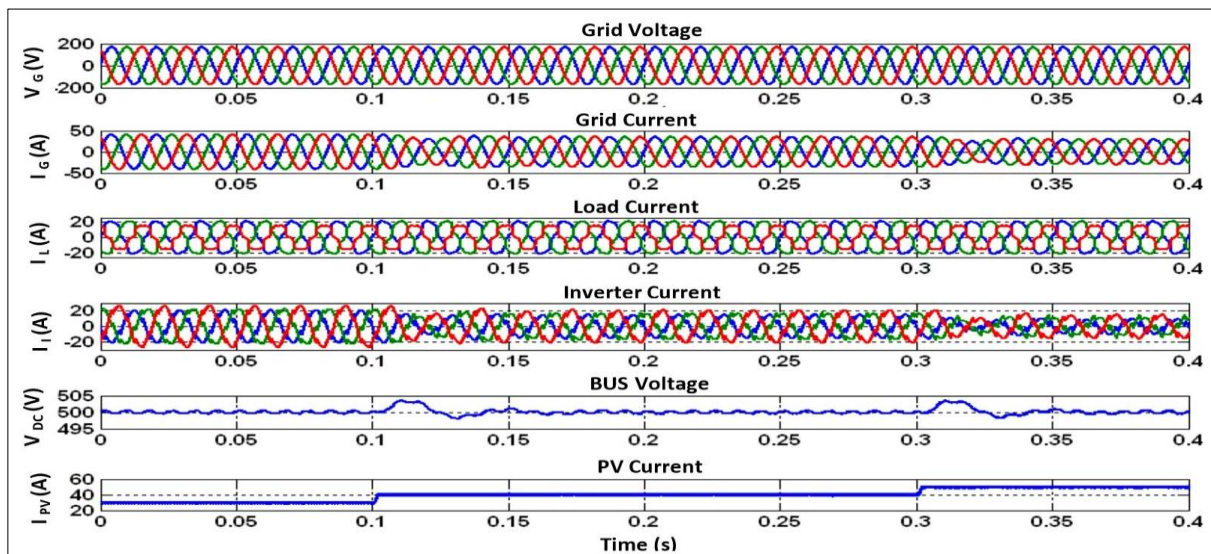
Figure 31. Dynamic response with a variation of solar radiation using a multi-variable filter.
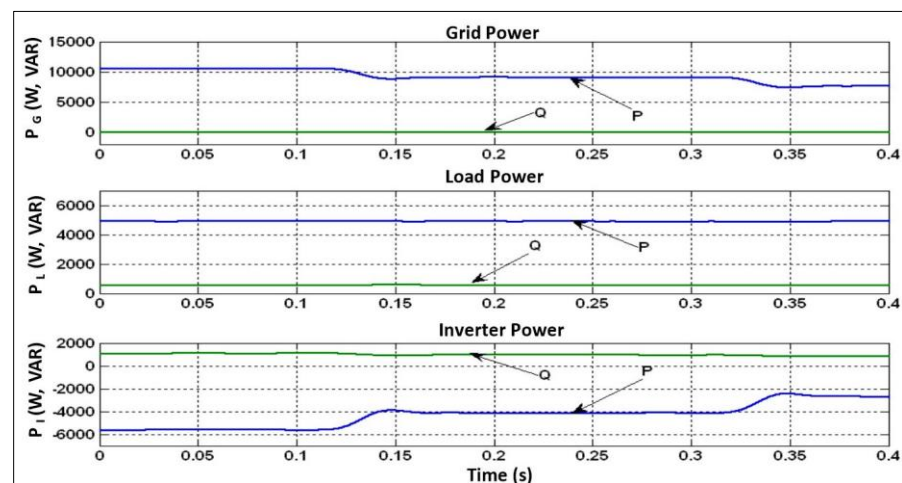

Figure 32. Power flow with a variation of solar radiation using a multi-variable filter.

4.3. Using Nonlinear Controller with Notch Filter

4.3.1. Assembled with Loads, Solar Radiation, and without a Battery System

The same simulation is carried out as in Section 4.1.1 by replacing the simple nonlinear controller of the inverter with the nonlinear controller with a notch filter. For the balanced load, no anomaly is seen in the grid current. In this case, the load is unbalanced. Thus inverter control system does not compensate for the currents correctly. Hence we need to introduce an inverse component in the control system to correct this abnormality. Adding this component gives us the expected results shown below.

We analyzed from Figure 33 that the grid current significantly decreased when solar radiation increased. In the absence of solar radiation, the current is in phase with the voltage. Therefore it supplies current. On the other side, the current is out of phase with the voltage with solar radiation. Thus it receives current. The V_{dc} is adequately regulated here. With G = 800 W/m², we observe a current of 40 A generated by the solar panel. Figure 34 shows that the power curves confirm that the load is supplied at 5000 W entirely by the grid, then the solar panel provides 6000 W under sunny conditions. At the same time, it can also feed the grid up to 1000 W. In Figure 35, we also observed a grid THD of 2.18% in a steady state.
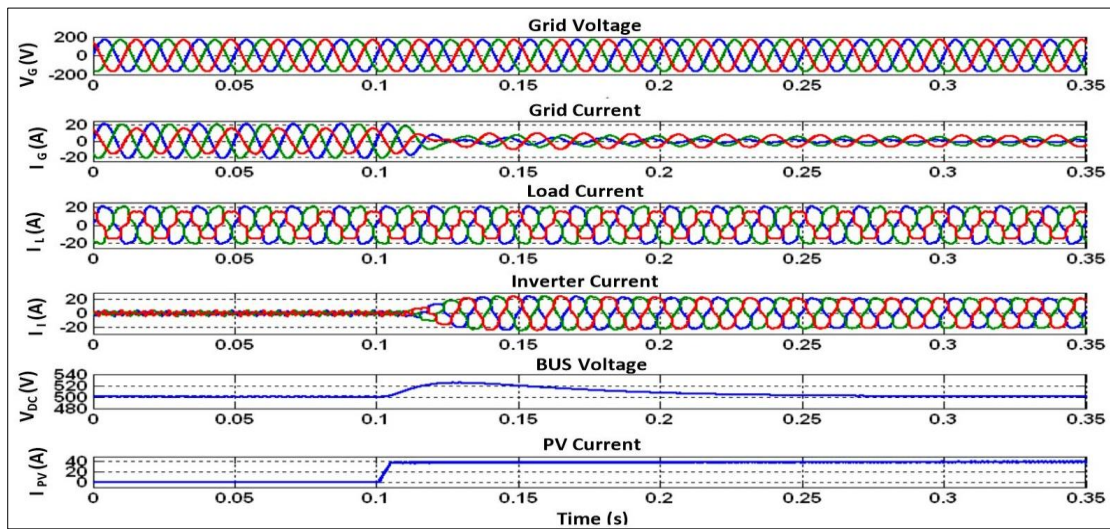
Figure 33. Dynamic response with solar radiation of $G = 800 \text{ W/m}^2$ using a notch filter.
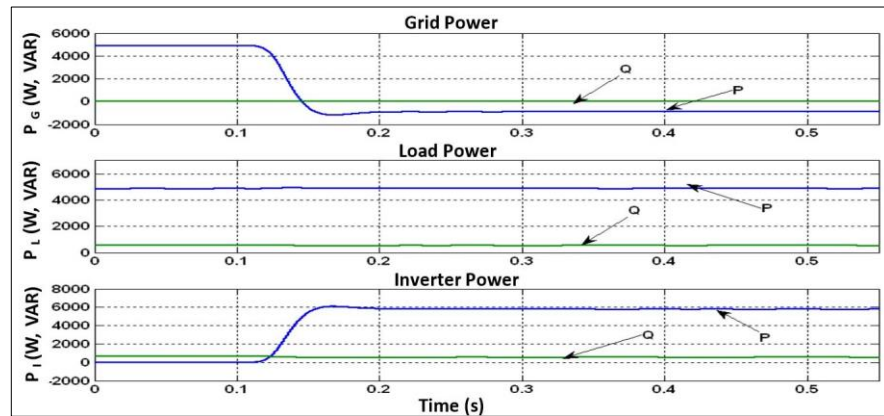

Figure 34. Power flow with solar radiation $G = 800 \text{ W/m}^2$ using a notch filter.
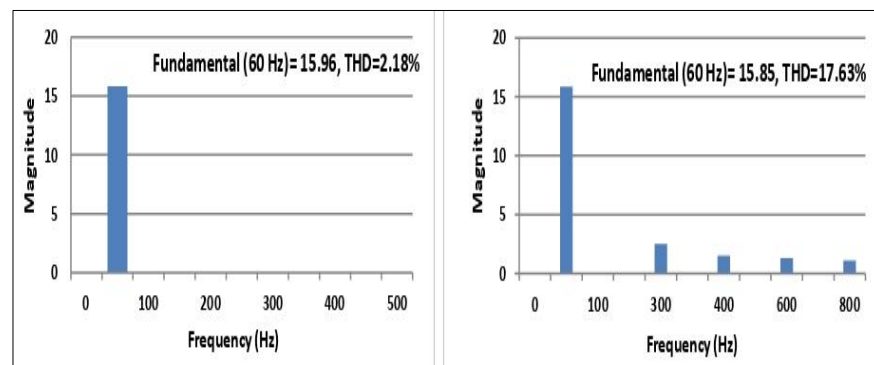

Figure 35. Harmonic spectrum of the grid and load current using a notch filter.

4.3.2. Assembled with Loads, Solar Radiation, and Variations of the Battery Charge

The same simulation is carried out as in Section 4.1.2 by replacing the simple nonlinear controller of the inverter with the nonlinear controller with a notch filter.

Figure 36 shows that the current in the inverter increases at $t = 0.1$ to 0.3 s because the battery discharges are shown in Figure 37. The results show phase opposition between the current and grid voltage, indicating that the grid receives power. Power curves confirmed that the inverter is negative when the battery absorbs current and positive when the battery discharges the current. In Figure 38, the curves relating to the battery indicate that when

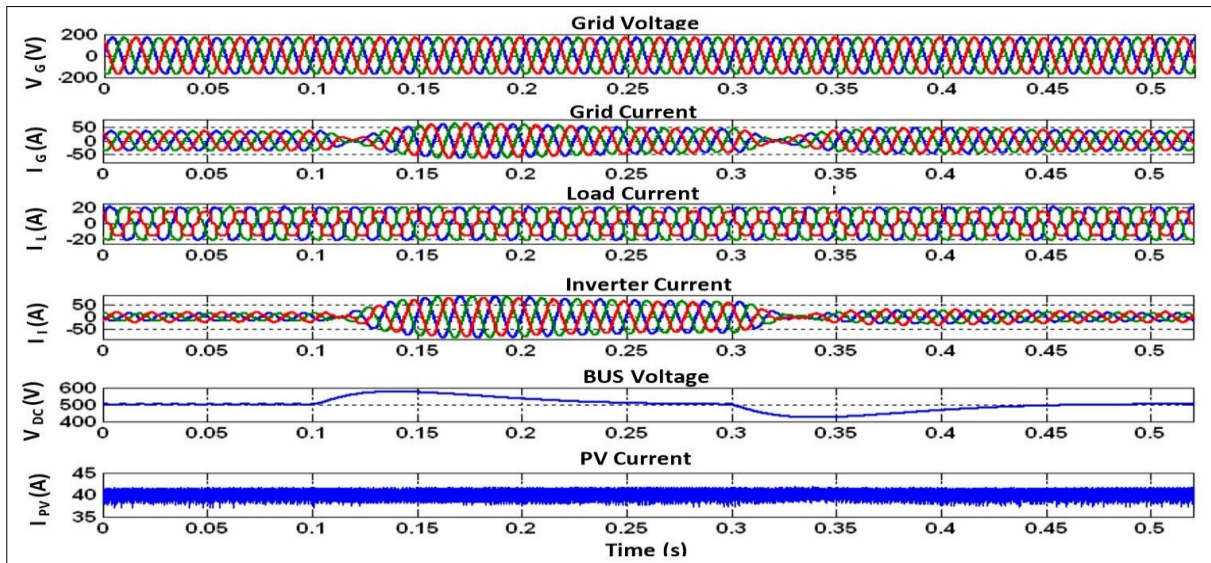the current imposed is negative, the battery is charged. When it is positive, it is discharged.

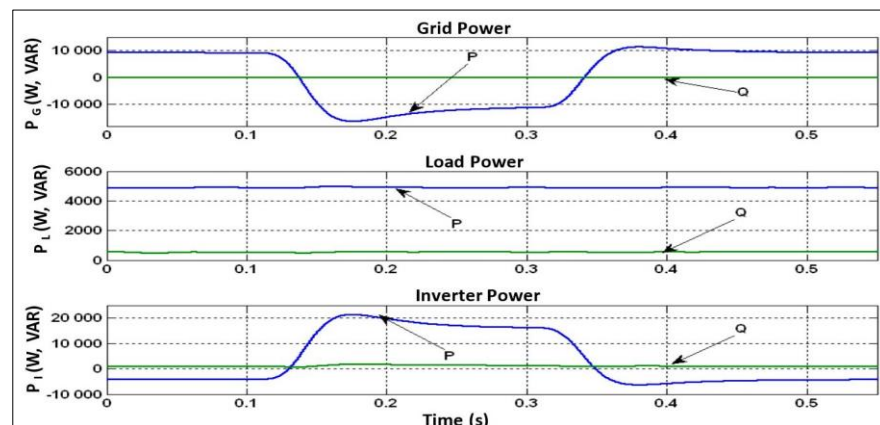**Figure 36.** Dynamic state response with battery charge variation using a notch filter.

Figure 37. Power flow with battery charge variation using a notch filter.
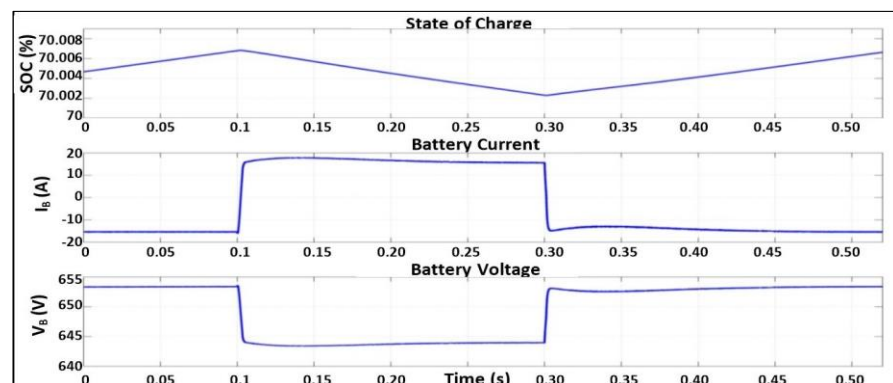

Figure 38. Battery state of charge using a notch filter.

4.3.3. Assembled with Solar Radiation, Battery Charge, and Variation of the Loads

The same simulation is carried out as in Section 4.1.3 by replacing the simple nonlinear controller of the inverter with the nonlinear controller with a notch filter. Here are the results we obtained.

From the above power curve, we observed the PV and grid that supply power to the load. With solar radiation of $G = 800$ W/m^2, the PV can't support the grid to supply power to the load. Figure 39 shows, when the load power increases at $t = 0.1$ s, the current in the grid increases due to the grid's power shown in Figure 40.
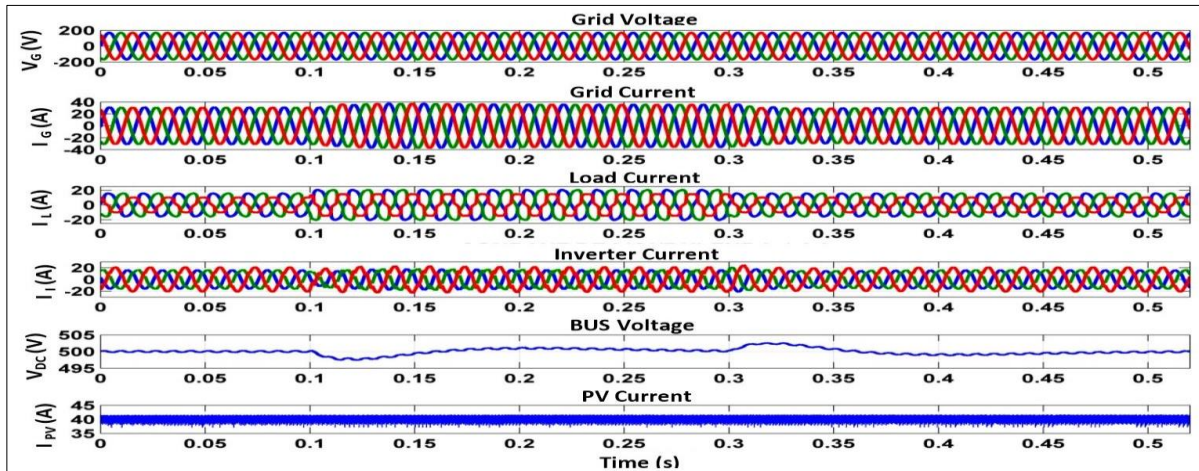

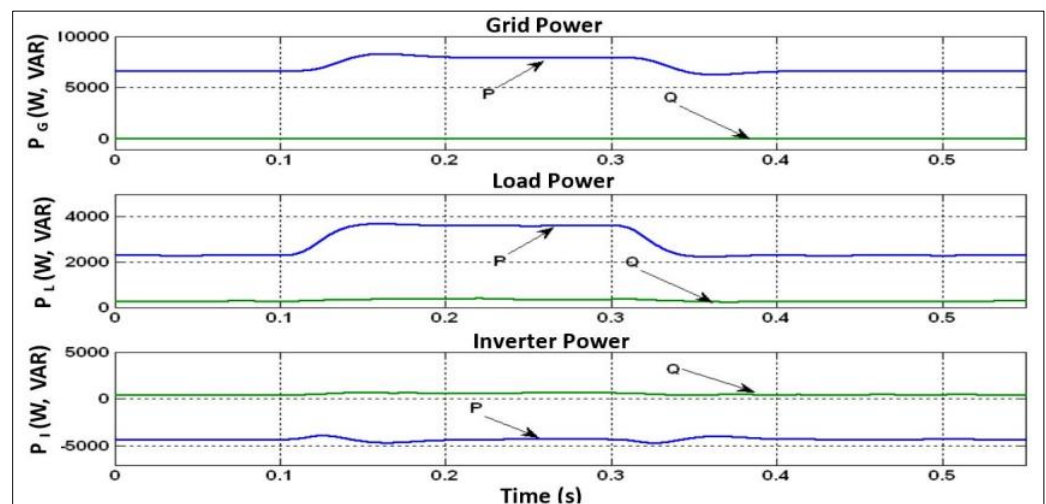**Figure 39.** Dynamic response with load variation using a notch filter.

Figure 40. Power Flow with load variation using a notch filter.

4.3.4. Assembled with Battery Charge, Load, and with Variation of the Solar Radiation

The same simulation is carried out as in Section 4.1.4 by replacing the simple nonlinear controller of the inverter with the nonlinear controller with a notch filter. Here are the results we obtained.

Figure 41 shows that the grid current decreases when solar radiation increases. This increment in solar radiation causes to increase in PV current from 25 A to 40 A and finally to 50 A. From the above power curve, we observed that the grid power decreases, inverter power increases and the load becomes constant, as shown in Figure 42.
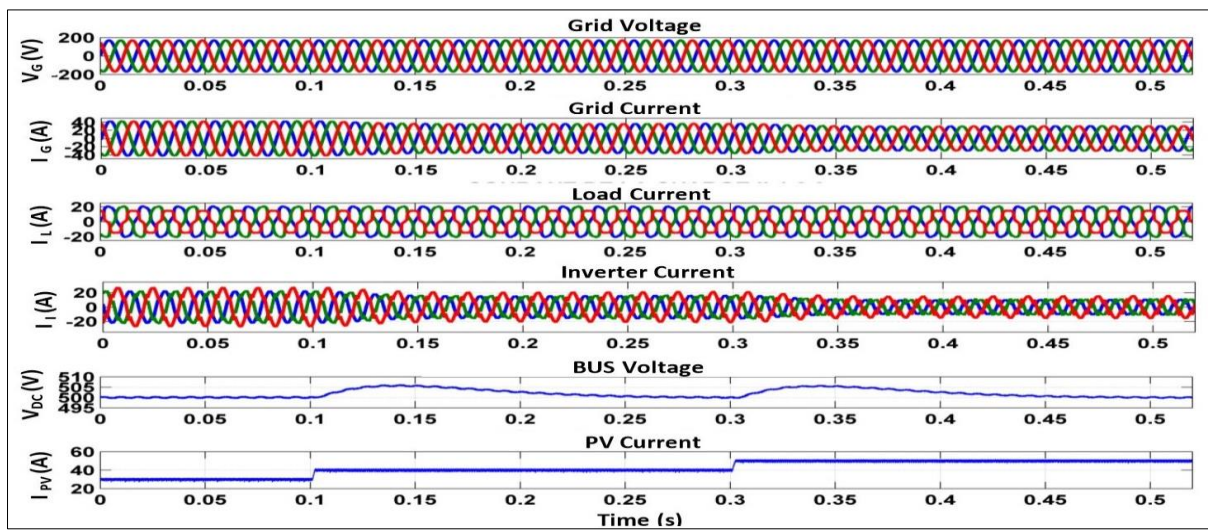
Figure 41. Dynamic response with a variation of solar radiation using a notch filter.
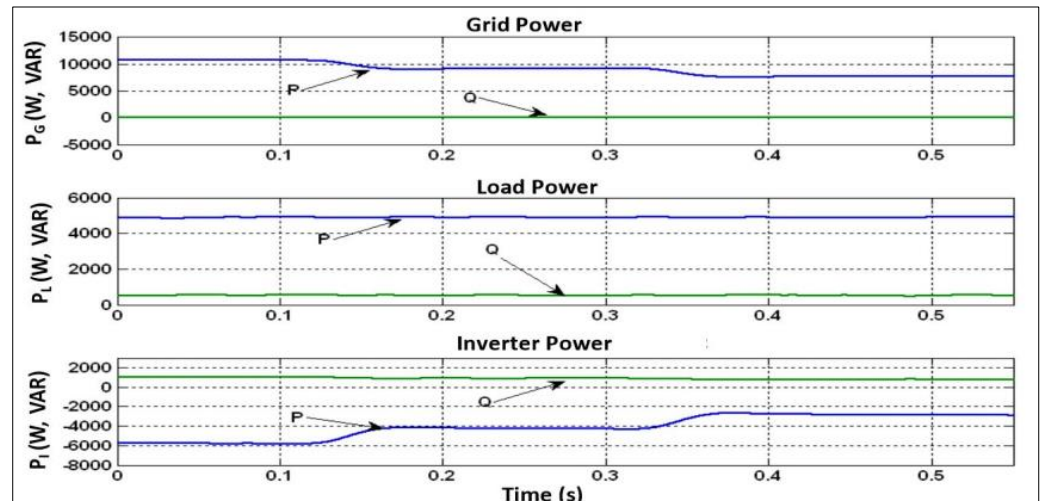

Figure 42. Power flow with a variation of solar radiation using a notch filter.

4.4. Using Nonlinear Controller without Filter

4.4.1. Assembled with Loads, Solar Radiation, and without a Battery System

The same simulation is carried out as in Section 4.1.1 by replacing the simple nonlinear controller of the inverter with the nonlinear controller without a filter. The dynamic responses with solar radiation of $G = 800$ W/m^2 without filter are shown in Figure 43. Figure 44 shows the power curves confirm that the load is supplied at 5000 W at first entirely by the grid, then the solar panel provides 6000 W under sunny conditions. At the same time, it can also feed the grid up to 1000 W. We also observed a grid THD of 1.48%, shown in Figure 45, in a steady state.

4.4.2. Assembled with Loads, Solar Radiation, and Variations of the Battery Charge

The same simulation is carried out as in Section 4.1.2 by replacing the simple nonlinear controller of the inverter with the nonlinear controller without a filter. The dynamic responses with solar radiation of $G = 800$ W/m^2 without filter are shown in Figure 46. The current in the inverter increases at $t = 0.1$ to 0.3 s because the battery discharges. The results show phase opposition between the current and the grid voltage, indicating that the grid receives power shown in Figure 47. Figure 48 shows the power curves confirming that

the inverter is negative when the battery absorbs current and positive when the battery discharges the current.
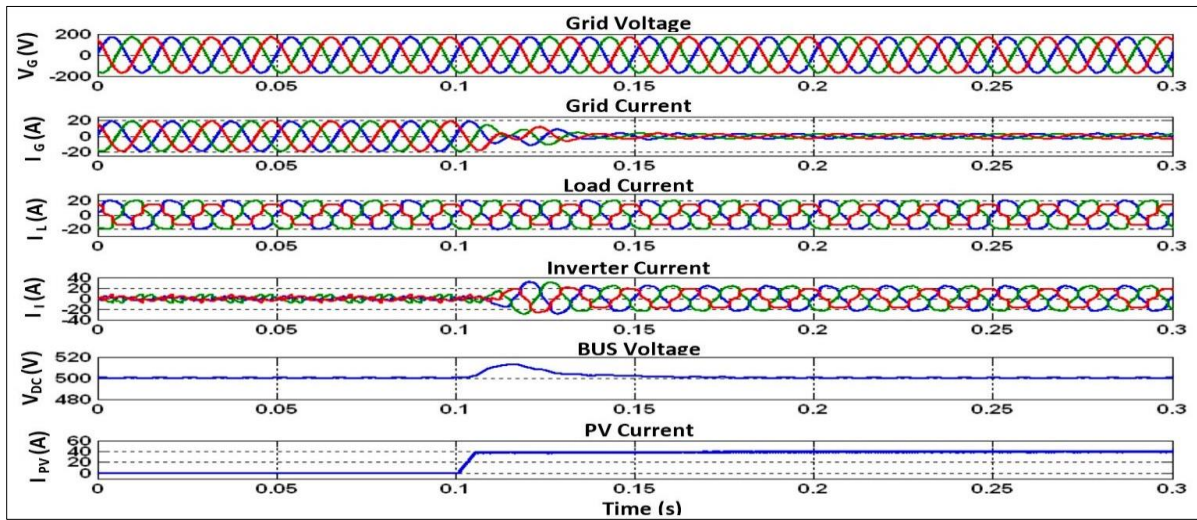

Figure 43. Dynamic response with solar radiation of $G = 800 \text{ W/m}^2$ without a filter.
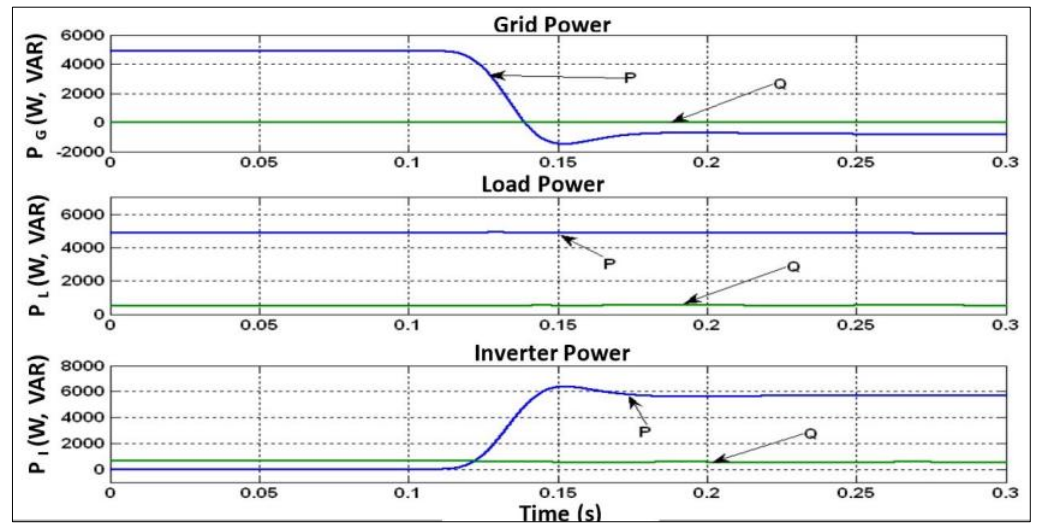

Figure 44. Power flow with solar radiation of $G = 800 \text{ W/m}^2$ without a filter.
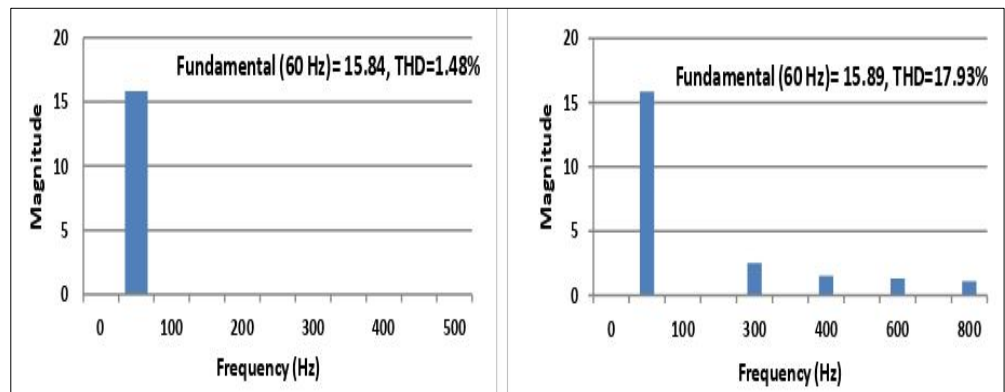

Figure 45. Harmonic spectrum of the grid and load current without a filter.

4.4.3. Assembled with Loads, Solar Radiation, and Variations of the Battery Charge

The same simulation is carried out as in Section 4.1.2 by replacing the simple nonlinear controller of the inverter with the nonlinear controller without a filter. The dynamic responses with solar radiation of $G = 800 \text{ W/m}^2$ without filter are shown in Figure 46. The current in the inverter increases at $t = 0.1$ to 0.3 s because the battery discharges. The results show phase opposition between the current and the grid voltage, indicating that the grid receives power shown in Figure 47. Figure 48 shows the power curves confirming that the inverter is negative when the battery absorbs current and positive when the battery discharges the current.
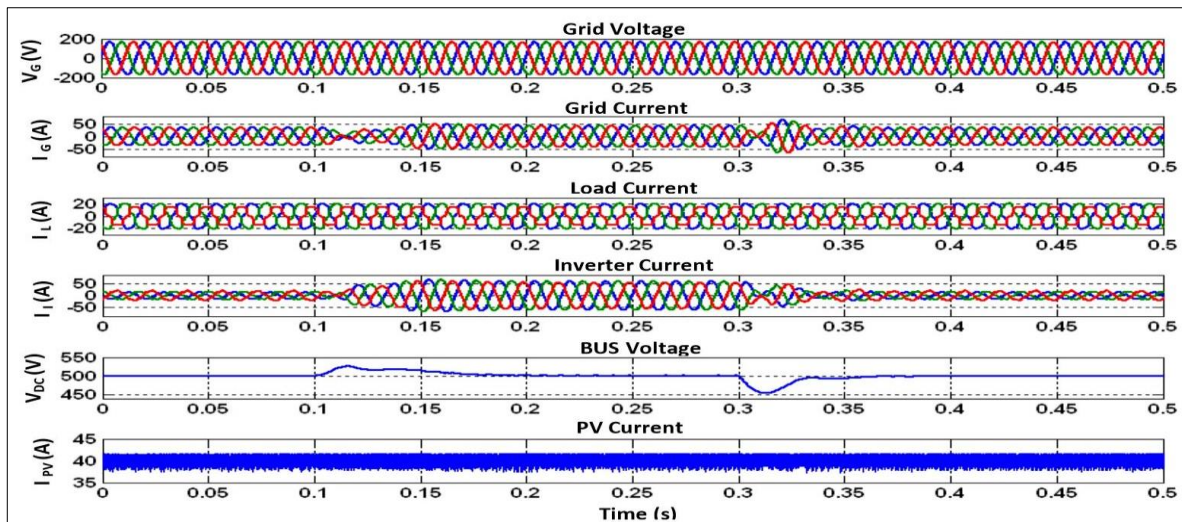

Figure 46. Dynamic State response with battery charge variation without a filter.
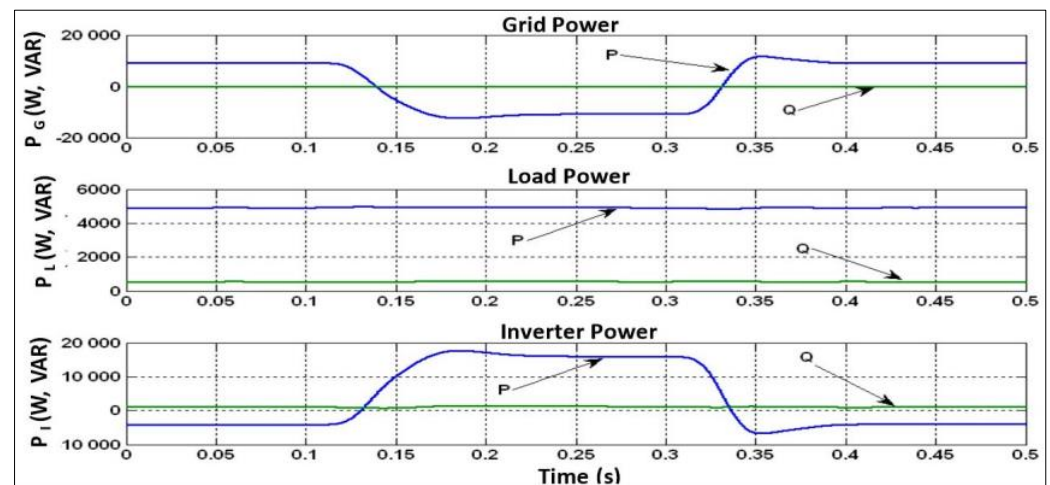

Figure 47. Dynamic state response with battery charge variation without a filter.

4.4.4. Assembled with Solar Radiation, Battery Charge, and Variation of the Loads

The same simulation is carried out as in Section 4.1.3 by replacing the simple nonlinear controller of the inverter with the nonlinear controller without a filter. Figure 49 shows the dynamic responses with solar radiation of $G = 800 \text{ W/m}^2$ without a filter. From the above power curve, we observed from Figure 50 that the PV and grid supply power to the load. When the load power increases at $t = 0.1$ s, the current in the grid increases due to the grid power. With solar radiation of $G = 800 \text{ W/m}^2$, the PV can't support the grid to supply the power to the load.
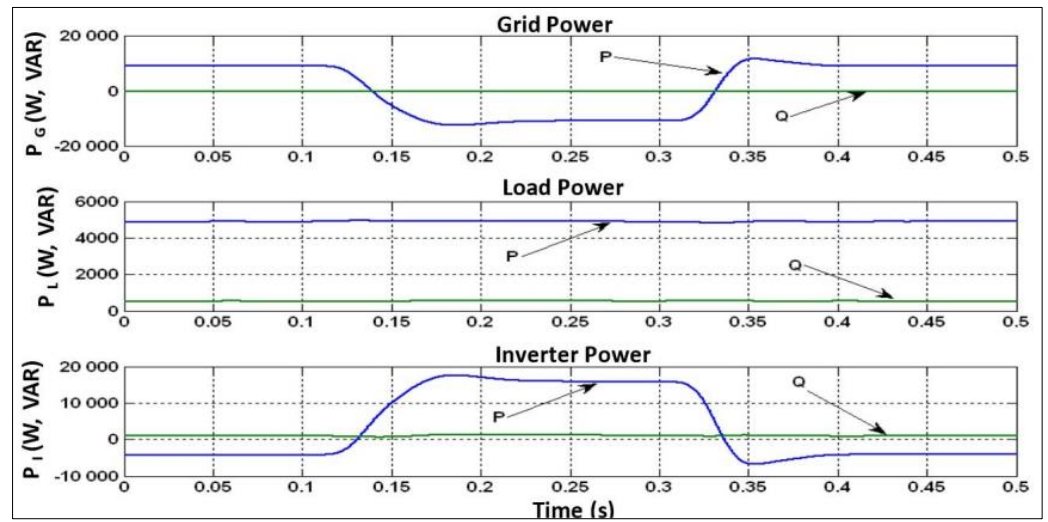
Figure 48. Battery state of charge using without a filter.
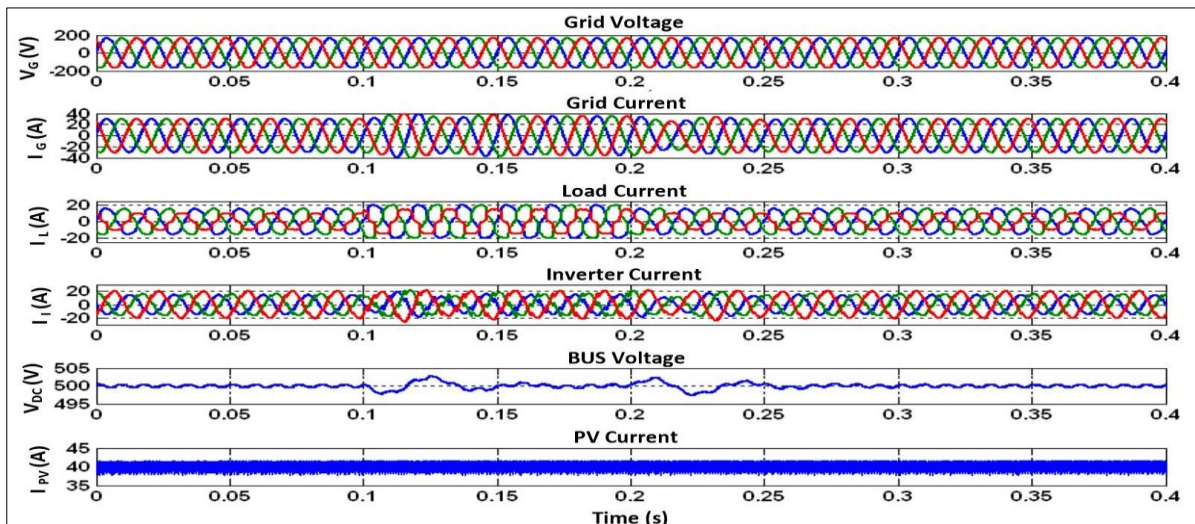
Figure 49. Dynamic response with load variation without a filter.
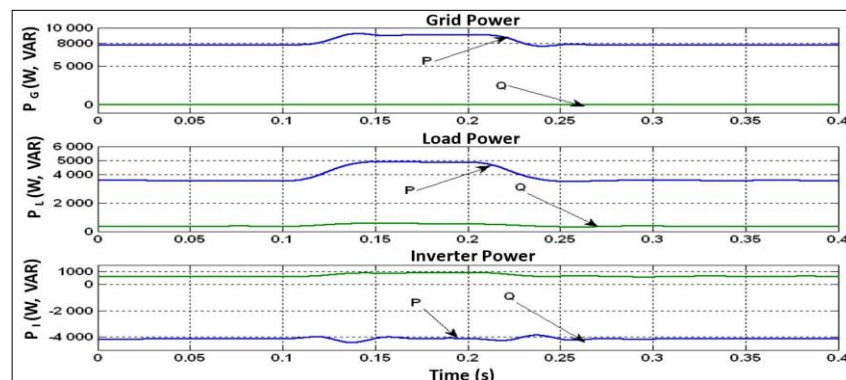
Figure 50. Power flow with load variation without a filter.

4.4.5. Assembled with Battery Charge, Load, and with Variation of the Solar Radiation

The same simulation is carried out as in Section 4.1.4 by replacing the simple nonlinear controller of the inverter with the nonlinear controller without a filter. The simulation results we obtained are shown as follows. Figure 51 shows that the grid current decreases

when solar radiation increases. This increment in solar radiation causes to increase in PV current from 25 A to 40 A and finally to 50 A. From the above power curve, we observed from Figure 52 that the grid power decreases, inverter power increases, and the load becomes constant.
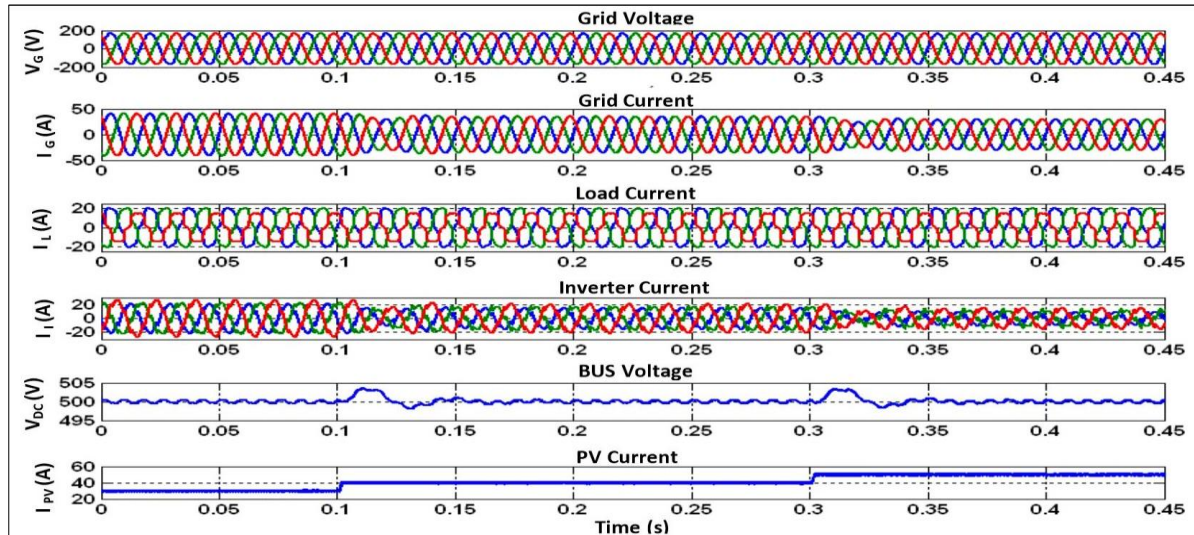

Figure 51. Dynamic responses with a variation of solar radiation without a filter.
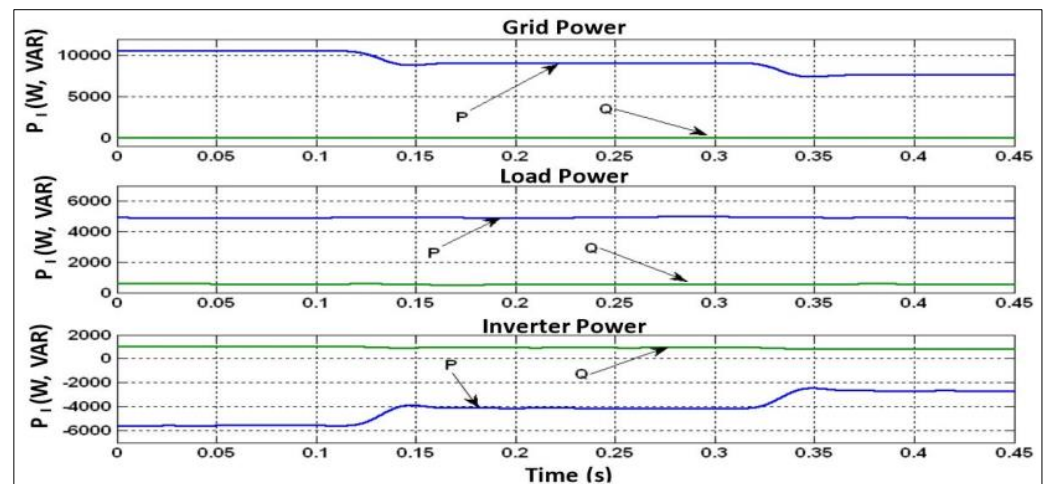
Figure 52. Power flow with a variation of solar radiation without a filter.

5. Comparison of Nonlinear Controllers with Various Filters

A final simulation is carried out to compare the performances of nonlinear controllers with various filters regarding the regulation of the DC bus. We simulate the overall system without the PV and battery for each controller, with a load variation from 4000 W to 5000 W between $t = 0.1$ s and 0.3 s. Figure 53 shows the result we obtained by grouping the curves for each of the controllers on the same figure:

Finally, let us note that the nonlinear control without a filter obtains the best regulation, followed by the simple nonlinear control (high pass filter) and the control with a multi-variable filter. The nonlinear control with a Notch filter has the worst result. Table 2 summarizes the performance of the different simulations of the various controllers used for the inverter.

Figure 53. DC bus regulation with various controllers.

Table 2. Ranking of controllers according to their performance.

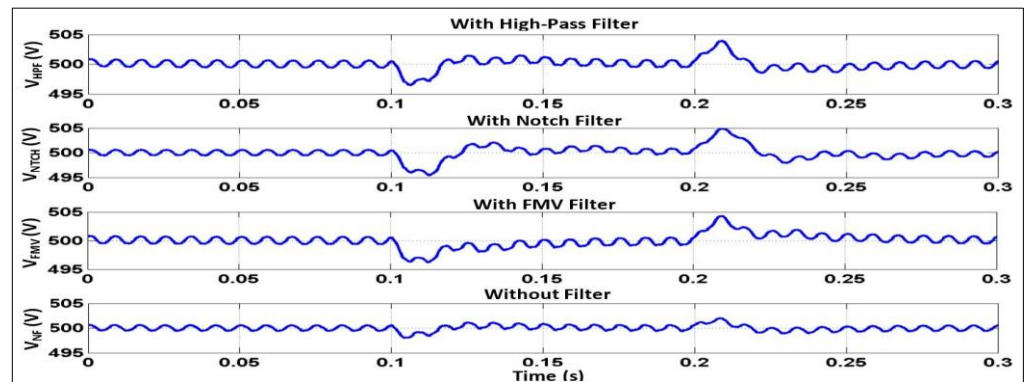| Types of Controllers	Simple Nonlinear Controller	Nonlinear Controller with Multi-Variable Filter	Nonlinear Controller with Notch Filter	Nonlinear Controller without Filter
THD of grid without the PV and Battery	1.43%	1.70%	1.61%	1.33%
Vdc Regulation Time with Load Variation	0.025 s	0.07 s	0.05 s	0.015 s
Vdc Exceeded with Load Variation	0.6%	0.8%	1%	0.2%

6. Conclusions

During this research, we presented a study on photovoltaic panels' connection to the electrical grid and a load. The operation of a storage device was also inserted into the assembly, which was carried out via Matlab simulation. The comprehensive study of solar energy has been carried out with the interface of a step-up converter equipped with a PI regulator and the MPPT implemented by the P&O method. At first, we connected the photovoltaic system and its storage device to the grid with an unbalanced nonlinear load. The inverter, which delivers alternating voltages and currents from a direct source of electrical energy, will play the role of interface between the panel and the grid. The inverter acts as a filter and makes it possible to compensate for the currents which pollute the network. Then several controllers were studied, modeled, and simulated. First, we use a simple nonlinear control with a traditional high-pass filter. Then we replaced it with a multi-variable filter and a Notch filter in another simulation. Finally, we used a nonlinear control without a filter. During our simulations, we obtained the expected results, proving each controller's performance. Therefore, we can affirm that this global topology is an exciting alternative for using solar energy, mainly its simplicity, performance, and speed. It turns out that during our simulations, the filterless nonlinear control obtained the best performance. For economic considerations, the energy produced by the solar panel should be prioritized by the grid and not the battery. We use an intelligent MPPT to get the maximum power from the connected solar panels with different capacities. Finally, we observed that the filterless nonlinear control provides the best results for THD correction (1.33%), V_{dc} regulation time with load variation (0.015 s), and V_{dc} exceeded with load variation (0.2%). The controller with the notch filter has the worst results for THD correction (1.61%), V_{dc} regulation time with load variation (0.05 s), and V_{dc} exceeded with load variation (1%). Following the V_{dc} regulation times, we see that the controller without the filter has the fastest and the notch controller has the slowest performance. It is noted that the controller with the notch filter has the worst results for the overshoot of the $V_{dc,}$

and the multi-variable filter has the poorest outcomes for the regulation speed of the V_{dc} (0.07 s) with the THD correction (1.70%). The simple nonlinear controller provides the THD correction (1.43%), V_{dc} regulation time with load variation (0.025 s), and V_{dc} exceeded with load variation (0.6%). Finally, the multi-variable filter is ranked fourth, the Notch filter is third, the simple nonlinear controller is second, and the nonlinear controller without the filter is ranked first. In summary, the nonlinear controller without a filter is the best for the operation. Concerning the quality of the electrical grid, the controllers used for the inverter ensure that the harmonic distortion rate remains below 5%, complying with the IEEE519-1992 standard for grid quality. This indicates that the proposed system maintains the required power quality levels while integrating renewable energy sources. This research highlights the prioritization of energy produced by the solar panel for the grid rather than the battery, considering economic factors. This approach optimizes the utilization of solar energy and enhances the cost-effectiveness of the system.

To continue this research work, the proposed system and controllers can be implemented in a real-world setup to verify the performance and effectiveness of the studied approaches under practical conditions. This will provide more robust and reliable results; The study by comparing the performance of the proposed controllers can be expanded with other existing control strategies for photovoltaic systems; The efficiency, stability, and dynamic response of different controllers can be evaluated to identify potential improvements or alternative approaches; Parameter tunings or advanced control algorithms such as Model Predictive Control (MPC) or Adaptive Control can be considered to enhance the response, accuracy, and stability of the system under varying operating conditions; The reliability and resilience of the proposed system can be assessed in the face of various disturbances and uncertainties. By considering these recommendations, the research work can be extended to further enhance the understanding, performance, and applicability of photovoltaic systems connected to the electrical grid, ultimately contributing to the advancement and adoption of renewable energy technologies.

Author Contributions: Conceptualization, M.J.R.; methodology, M.J.R.; software, M.J.R.; validation, T.T. and M.L.D.; data curation, M.J.R.; writing—original draft, M.J.R.; writing—review and editing, M.J.R., T.T., M.L.D. and I.M.; supervision, T.T. and M.L.D.; funding acquisition, T.T. All authors have read and agreed to the published version of the manuscript.

Data Availability Statement: Data is contained within the article.

Conflicts of Interest: The authors declare no conflict of interest.

References

1. Ajabnoor, A.; Kwasinski, A. Photovoltaic Maximum Power Point Tracker for a Multiple-Input SEPIC Under Partial Shading Condition. In Proceedings of the 2022 IEEE 13th International Symposium on Power Electronics for Distributed Generation Systems (PEDG), Kiel, Germany, 26–29 June 2022; pp. 1–6. [CrossRef]
2. Rahman, M.J.; Tafticht, T.; Doumbia, M.L. Power Stability and Frequency Control Techniques of DG for a High Penetration Wind-Based Energy Storage System Using Integral–Derivative Controller. *IEEE Can. J. Electr. Comput. Eng.* **2022**, *45*, 232–241. [CrossRef]
3. Rahman, M.J.; Tafticht, T.; Doumbia, M.L.; Mutombo, N.M.-A. Dynamic Stability of Wind Power Flow and Network Frequency for a High Penetration Wind-Based Energy Storage System Using Fuzzy Logic Controller. *Energies* **2021**, *14*, 4111. [CrossRef]
4. Purevdorj, G.; Enkjargal, K. Ecological, economic and social aspects from the renewable energy and energy conservation. In Proceedings of the 2007 International Forum on Strategic Technology, Ulaanbaatar, Mongolia, 3–6 October 2007; pp. 20–23. [CrossRef]
5. Bineeta, M.; Das, D. Multi-objective dynamic and static reconfiguration with optimized allocation of PV-DG and battery energy storage system. *Renew. Sustain. Energy Rev.* **2020**, *124*, 109777.
6. Kermadi, M.; Salam, Z.; Ahmed, J.; Berkouk, E.M. A High-Performance Global Maximum Power Point Tracker of PV System for Rapidly Changing Partial Shading Conditions. *IEEE Trans. Ind. Electron.* **2021**, *68*, 2236–2245. [CrossRef]
7. Hernández, J.C.; Sanchez-Sutil, F.; Muñoz-Rodríguez, F.J. Design criteria for the optimal sizing of a hybrid energy storage system in PV household-prosumers to maximize self-consumption and self-sufficiency. *Energy* **2019**, *186*, 115827. [CrossRef]

8. Li, X.; Wang, L.; Yan, N.; Ma, R. Cooperative Dispatch of Distributed Energy Storage in Distribution Network With PV Generation Systems. *IEEE Trans. Appl. Supercond.* **2021**, *31*, 0604304. [CrossRef]

9. Alivarani, M.; Nayak, B.; Das, P.; Mohanty, K.B. A review on MPPT techniques of PV system under partial shading condition. *Renew. Sustain. Energy Rev.* **2017**, *80*, 854–867.

10. Winston, D.; Prince, S.; Kumaravel, B.; Kumar, P.; Devakirubakaran, S. Performance improvement of solar PV array topologies during various partial shading conditions. *Solar Energy* **2020**, *196*, 228–242. [CrossRef]

11. Bidram, A.; Davoudi, A.; Balog, R.S. Control and Circuit Techniques to Mitigate Partial Shading Effects in Photovoltaic Arrays. *IEEE J. Photovolt.* **2012**, *2*, 532–546. [CrossRef]

12. Teshome, D.F.; Lee, C.H.; Lin, Y.W.; Lian, K.L. A Modified Firefly Algorithm for Photovoltaic Maximum Power Point Tracking Control Under Partial Shading. *IEEE J. Emerg. Sel. Top. Power Electron.* **2017**, *5*, 661–671. [CrossRef]

13. Zengin, S.; Boztepe, M. Modified dual active bridge photovoltaic inverter for solid state transformer applications. In Proceedings of the 2014 International Symposium on Fundamentals of Electrical Engineering (ISFEE), Bucharest, Romania, 28–29 November 2014; pp. 1–4. [CrossRef]

14. Ishaque, K.; Salam, Z. A Review of Maximum Power Point Tracking Techniques of PV System for Uniform Insolation and Partial Shading Condition. *Renew. Sustain. Energy Rev.* **2013**, *19*, 475–488. [CrossRef]

15. Adam, G.P.; Alajmi, B.; Ahmed, K.H.; Finney, S.J.; Williams, B.W. New flying capacitor multilevel converter. In Proceedings of the 2011 IEEE International Symposium on Industrial Electronics, Gdansk, Poland, 27–30 June 2011; pp. 335–339. [CrossRef]

16. Roberts, M.B.; Bruce, A.; MacGill, I. Impact of shared battery energy storage systems on photovoltaic self-consumption and electricity bills in apartment buildings. *Appl. Energy* **2019**, *245*, 78–95. [CrossRef]

17. Sahu, H.S.; Nayak, S.K.; Mishra, S. Maximizing the Power Generation of a Partially Shaded PV Array. *IEEE J. Emerg. Sel. Top. Power Electron.* **2016**, *4*, 626–637. [CrossRef]

18. Lin, H.; Veda, S.S.; Shukla, S.S.; Mili, L.; Thorp, J. GECO: Global Event-Driven Co-Simulation Framework for Interconnected Power System and Communication Network. *IEEE Trans. Smart Grid* **2012**, *3*, 1444–1456. [CrossRef]

19. Okan, B.; Özkaya, B. Analysis and comparison of different PV array configurations under partial shading conditions. *Solar Energy* **2018**, *160*, 336–343.

20. Wang, Y.; Lin, X.; Kim, Y.; Chang, N.; Pedram, M. Architecture and Control Algorithms for Combating Partial Shading in Photovoltaic Systems. *IEEE Trans. Comput.-Aided Des. Integr. Circuits Syst.* **2014**, *33*, 917–930. [CrossRef]

21. Teo, J.C.; Tan, R.H.; Mok, V.H.; Ramachandaramurthy, V.K.; Tan, C. Impact of partial shading on the PV characteristics and the maximum power of a photovoltaic string. *Energies* **2018**, *11*, 1860. [CrossRef]

22. Rahmann, C.; Vittal, V.; Ascui, J.; Haas, J. Mitigation Control Against Partial Shading Effects in Large-Scale PV Power Plants. *IEEE Trans. Sustain. Energy* **2016**, *7*, 173–180. [CrossRef]

23. Xiao, W.; El Moursi, M.S.; Khan, O.; Infield, D. Review of grid-tied converter topologies used in photovoltaic systems. *IET Renew. Power Gener.* **2016**, *10*, 1543–1551. [CrossRef]

24. Tafticht, T.; Tchakala, M.; Rahman, M.J. GMPPT Approach for Photovoltaic Systems under Partial Shading Conditions Using Genetic Algorithm. *Int. J. Power Electron. Drive Syst.* **2022**, *13*, 1238–1245. [CrossRef]

25. Salem, R.; Mendalek, N.; Al-Haddad, K. Experimental design of a nonlinear control technique for three-phase shunt active power filter. *IEEE Trans. Ind. Electron.* **2010**, *57*, 3364–3375.

26. Ahmed, B.; Hamadi, A.; Ndtoungou, A.; Javadi, A.; Rahmani, S.; Al-Haddad, K. Modified droop control to improve performances of two single-phase parallel inverters. In Proceedings of the IECON 2017-43rd Annual Conference of the IEEE Industrial Electronics Society, Beijing, China, 29 October–1 November 2017; IEEE: New York City, NY, USA, 2017; pp. 6470–6475.

27. Ali, E.; Cingoz, F.; Sozer, Y. Smart loads management using droop-based control in integrated microgrid systems. *IEEE J. Emerg. Sel. Top. Power Electron.* **2017**, *5*, 1142–1153.

28. Egwebe, M.; Fazeli, M.; Igic, P.; Holland, P.M. Implementation and Stability Study of Dynamic Droop in Islanded Microgrids. *IEEE Trans. Energy Convers.* **2016**, *31*, 821–832. [CrossRef]

29. Abdelsalam, K.; Massoud, A.M.; Ahmed, S.; Enjeti, P.N. High-Performance Adaptive Perturb and Observe MPPT Technique for Photovoltaic-Based Microgrids. *IEEE Trans. Power Electron.* **2011**, *26*, 1010–1021. [CrossRef]

30. Banu, I.V.; Istrate, M. Comparative Analysis of the Perturb-and-Observe and Incremental Conductance MPPT Methods. In Proceedings of the 2013 8th International Symposium on Advanced Topics in Electrical Engineering (ATEE), Bucharest, Romania, 23–25 May 2013. [CrossRef]

31. Park, C.-Y.; Hong, S.-H.; Lim, S.-C.; Song, B.-S.; Park, S.-W.; Huh, J.-H.; Kim, J.-C. Inverter Efficiency Analysis Model Based on Solar Power Estimation Using Solar Radiation. *Processes* **2020**, *8*, 1225. [CrossRef]

32. Blanco, H.; Faaij, A. A review at the role of storage in energy systems with a focus on Power to Gas and long-term storage. *Renew. Sustain. Energy Rev.* **2018**, *81 Pt 1*, 1049–1086. [CrossRef]

33. Du, Y.; Lu, D.D.-C.; James, G.; Cornforth, D.J. Modeling and analysis of current harmonic distortion from grid connected PV inverters under different operating conditions. *Solar Energy* **2013**, *94*, 182–194. [CrossRef]

34. Al-Shetwi, A.Q.; Hannan, M.A.; Jern, K.P.; Alkahtani, A.A.; PG Abas, A.E. Power Quality Assessment of Grid-Connected PV System in Compliance with the Recent Integration Requirements. *Electronics* **2020**, *9*, 366. [CrossRef]

35. Rocchetta, R. Enhancing the resilience of critical infrastructures: Statistical analysis of power grid spectral clustering and post-contingency vulnerability metrics. *Renew. Sustain. Energy Rev.* **2022**, *159*, 112185. [CrossRef]

36. Chim, C.S.; Neelakantan, P.; Yoong, H.P.; Teo, K.T. Fuzzy Logic Based MPPT for Photovoltaic Modules Influenced by Solar Irradiation and Cell Temperature. In Proceedings of the 13th International UkSim Conference on Modelling and Simulation, Cambridge, UK, 30 March–1 April 2011; pp. 376–381. [CrossRef]
37. Karimi-Ghartemani, M.; Mokhtari, H. Extraction of Harmonics and Reactive Current for Power Quality Enhancement. In Proceedings of the 2006 IEEE International Symposium on Industrial Electronics, Montreal, QC, Canada, 9–13 July 2006; pp. 1673–1678. [CrossRef]
38. Chaoui, A.; Gaubert, J.-P.; Bouafia, A. Experimental Validation of Active Power Filtering with a Simple Robust Control. *Electr. Power Compon. Syst.* **2016**, *44*, 1163–1176. [CrossRef]
39. Rampradesh, T.; Rajan, C.C.A. Performance assessment of NMPC based MPPT controller and extended Kalman filter for a Wind/PV hybrid system. In Proceedings of the 2021 Fourth International Conference on Electrical, Computer and Communication Technologies (ICECCT), Erode, India, 15–17 September 2021; pp. 1–4. [CrossRef]